

See discussions, stats, and author profiles for this publication at: <https://www.researchgate.net/publication/225131556>

# Effect of Sc on Aging Kinetics in a Direct Chill Cast Al-Zn-Mg-Cu Alloy

ARTICLE *in* METALLURGICAL AND MATERIALS TRANSACTIONS A · MAY 2008

Impact Factor: 1.73 · DOI: 10.1007/s11661-008-9485-6

---

CITATIONS

16

---

READS

37

3 AUTHORS, INCLUDING:



Oleg Senkov

UES, Inc.

267 PUBLICATIONS 3,792 CITATIONS

SEE PROFILE

# Effect of Sc on Aging Kinetics in a Direct Chill Cast Al-Zn-Mg-Cu Alloy

O.N. SENKOV, S.V. SENKOVA, and M.R. SHAGIEV

The effect of Sc additions on precipitation strengthening in a direct chill (DC) cast Al-Zn-Mg-Cu alloy was studied after natural and artificial aging. The microhardness, room temperature (RT) mechanical properties, and phase composition of the alloys were determined after different steps of aging. The strengthening mechanisms were discussed. It was shown that minor additions of Sc increased the strength of the Al-Zn-Mg-Cu alloy after casting and solution heat treatment, due to the precipitation of fine coherent  $\text{Al}_3(\text{Sc,Zr})$  particles. An analysis of the aging kinetics revealed that Sc had no effect on the natural aging, which was controlled by the formation and growth of Guinier–Preston (GP) I zones. On the other hand, the Sc additions accelerated the aging process at 120 °C and 150 °C within a period of time of the formation and growth of GP II zones and  $\eta'$  particles. It was concluded that the presence of Sc accelerated the formation and growth of GP II zones in the Al-Zn-Mg-Cu alloys, which led to the earlier precipitation of the  $\eta'$  phase. However, at longer aging times at 120 °C and 150 °C, the aging response of the Sc-containing alloys slowed down, due to faster coarsening of the  $\eta'$  particles and their transformation into  $\eta$  particles. A model of the formation of vacancy-rich clusters (VRCs), precursors to GP zones, in the Al-Zn-Mg-based alloys was proposed. According to this model, the observed effects of Sc on aging are the result of the Sc-induced increase in the number density of the GP II clusters and the concentration of quenched-in solute-bound excess vacancies.

DOI: 10.1007/s11661-008-9485-6

© The Minerals, Metals & Materials Society and ASM International 2008

## I. INTRODUCTION

NEWER materials with high specific properties and low cost are always in high demand in the aerospace industry. Al-Zn-Mg-Cu alloys of the 7000 series have the highest strength among all commercial Al alloys.<sup>[1]</sup> Their strength is mainly controlled by the precipitation reactions accompanying heat treatment. The precipitation during aging of the supersaturated solid solution in these alloys is recognized to occur in the following sequence (with an increase in the aging time and/or temperature):<sup>[2]</sup>

supersaturated solid solution

→ Guinier – Preston (GP) zones

→ metastable  $\eta'$  or  $T'$

→ equilibrium  $\eta(\text{MgZn}_2)$  or  $T(\text{Mg}_{32}[\text{Al,Zn}]_{49})$

The interfacial energy between the coherent GP zones and the matrix is low, so that zones of a very small size can form. The metastable  $\eta'$  and  $T'$  phases are semicoherent with the matrix and have higher interfacial energies and,

therefore, require larger critical nucleus sizes to form and grow. The  $\eta'$ <sup>[3]</sup> and  $T'$ <sup>[4]</sup> phases have hexagonal crystal structures. The formation of the incoherent equilibrium  $\eta$  and  $T$  phases, which have a hexagonal and a cubic crystal structure,<sup>[5]</sup> respectively, generally coincides with overaging, *i.e.*, with a decrease in both strength and hardness. The  $\eta'$  and  $\eta$  phases are formed during aging of the alloys having high Zn:Mg ratios, while the  $T'$  and  $T$  phases are formed in the alloys with moderate to low Zn:Mg ratios (generally less than 3:1).

Two types of GP zones, GP I and GP II, have recently been identified.<sup>[6–8]</sup> The GP I zone nucleates on Mg-Zn clusters in the temperature range below ~100 °C, has a spherical shape of up to 6 nm in diameter, and dissolves in a range from 100 °C to 140 °C, depending on the holding time.<sup>[7,9,10]</sup> The Mg:Zn ratio in GP I is about 1:2,<sup>[11]</sup> and the atoms are internally ordered on  $\{100\}_{\text{Al}}$  planes.<sup>[7]</sup> The GP II zones seem to nucleate on vacancy-rich clusters (VRCs) that are formed during quenching after solution treatment at temperatures above 450 °C.<sup>[12]</sup> These clusters are more enriched with Zn (Mg:Zn ratio is ~1:5 to 1:4<sup>[11]</sup>) and start to dissolve at higher temperatures than GP I.<sup>[7–9,11]</sup> The morphology of GP II has not been well defined. High-resolution transmission electron microscopy (HRTEM) images indicate that these are disk- or platelike zones a few atoms thick located on  $\{111\}_{\text{Al}}$  planes.<sup>[7]</sup> On the other hand, three-dimensional atom probe (3DAP) analysis identifies GP II as spherical precipitates, similar to GP I.<sup>[6,8]</sup> At longer aging times, both GP I and GP II can transform to  $\eta'$ .<sup>[7–11,13]</sup> The  $\eta'$  precipitates may also

O.N. SENKOV, Senior Scientist, and S.V. SENKOVA, Junior Scientist, are with UES, Inc., Dayton, OH 45432-1894. Contact e-mail: oleg.senkov@wpafb.af.mil M.R. SHAGIEV, Materials Scientist, formerly with UES, Inc., is with the Institute for Metals Superplasticity Problems, Russian Academy of Sciences, Ufa 450001, Russia.

Manuscript submitted April 4, 2007.

Article published online March 7, 2008

nucleate directly from the supersaturated solid solution. The addition of Cu to Al-Zn-Mg alloys has been reported to stabilize the GP zones and  $\eta'$  particles (*i.e.*, Cu increases the solvus temperatures and hinders coarsening of these particles)<sup>[8,14,15]</sup> and suppress formation of the  $T'$  phase in favor of  $\eta$ .<sup>[14]</sup> A trace addition of Zr to an Al-5.75Zn-0.74Mg alloy (composition is in weight percent) has been reported in earlier work<sup>[16,17]</sup> to retard GP zones and  $\eta'$  formation and slow down  $\eta$  precipitation. This was attributed to an increase in the number of vacancy sinks and vacancy traps in the wrought microstructure of the Zr-containing alloy. On the other hand, the results of recent work<sup>[15]</sup> have shown that the addition of 0.16 pct Zr to an Al-5.5Zn-1.24Mg alloy slows the formation of GP II zones at room temperature (RT) within the first seven days after solution treatment, but it accelerates their formation at longer times and during artificial aging at 100 °C and leads to a reduction in the amount of  $\eta'$  formed during subsequent aging. The kinetics of the formation of GP I zones during aging at both RT and 100 °C was not affected by Zr.<sup>[15]</sup>

The strength of the Al-Zn-Mg-Cu alloys generally increases with an increase in the amount of Zn and Mg; however, when the amount of Zn exceeds 7 to 8 pct, the alloys become prone to hot tearing during casting and hot cracking during rapid cooling from a processing temperature. The 7000-series alloys generally have low ductility and low fracture strength in the as-cast condition. Proper thermomechanical treatment, which may involve hot working, such as forging, hot rolling, or extrusion, significantly improves the mechanical properties.<sup>[2]</sup> Fortunately, the fracture-related properties of these alloys can be considerably improved by small additions of Sc and Zr,<sup>[18,19]</sup> which enable a superior combination of higher strength levels and acceptable ductility, both in wrought<sup>[20,21]</sup> and cast<sup>[22,23]</sup> conditions. The beneficial effects from additions of Sc and Zr to different aluminum alloys are discussed in a recent review.<sup>[24]</sup> These are grain refinement during casting; a reduction in quench sensitivity; an increase in the strength and microstructure stability, due to the formation of fine coherent  $\text{Al}_3(\text{Sc,Zr})$  particles; the inhibition of recrystallization during hot working and heat treatment; an improvement in weldability; *etc.*

It has recently been found<sup>[22,23]</sup> that small additions of Sc and Zr can improve the tensile strength and ductility of cast-7000 alloys to the levels typical of the properties of the wrought alloys. The improved ductility was explained by the following: (1) Sc-induced grain refinement during casting,<sup>[22,23]</sup> (2) inhibition of the formation of twinned columnar dendrites,<sup>[23]</sup> and (3) a more homogeneous microstructure after casting.<sup>[23]</sup> The increased strength values were related to the formation of the fine coherent  $\text{Al}_3\text{Sc}$  particles. Recent Small Business Innovative Research (SBIR) studies<sup>[25]</sup> have also shown that the Sc-containing Al-Zn-Mg-Cu alloys of the SSA-alloy series being developed by UES, Inc.<sup>[26,27]</sup> (Dayton, OH) have a fluidity index similar to that of A356-cast alloy, which is one of the best Al-cast alloys. The development of the Sc-containing high-strength Al-Zn-Mg-Cu cast alloys with mechanical properties similar to

those of the commercial wrought Al alloys should afford benefits in both cost and energy savings.

There is very limited and contradictory information on the effect of Sc on the precipitation strengthening of the Al-Zn-Mg(-Cu) alloys.<sup>[24]</sup> There are reports that the Sc addition to these alloys slows,<sup>[28]</sup> accelerates,<sup>[19,21]</sup> or does not affect<sup>[29]</sup> the precipitation of  $\eta'$  particles. During solution treatment prior to aging, coarsening of the  $\text{Al}_3\text{Sc}$  particles should occur, which also may affect the final properties. This has not been properly addressed in the literature for the Al-Zn-Mg-based alloys. The objective of the present work was, therefore, to study the effect of the Sc addition and heat-treatment parameters on the microstructure and mechanical properties of a direct-chill (DC)-cast Al-Zn-Mg-Cu alloy, with primary attention on aging kinetics.

## II. EXPERIMENTAL

Four Sc-modified Al-Zn-Mg-Cu alloys having designations and compositions shown in Table I were produced by semicontinuous DC casting as 76-mm-diameter billets. The alloys have the same nominal compositions, but have different Sc concentrations of 0, 0.18, 0.38, and 0.49 pct Sc (all compositions are in weight percent). The microstructure, microhardness, and tensile properties of these alloys were studied in as-cast, solution-treated, and aged conditions. A PHILIPS\* CM200 transmission

---

\*PHILIPS is a trademark of Philips Electronic Instruments Corp., Mahwah, NJ.

---

electron microscope, operating at an accelerating voltage of 200 kV, was used for microstructural analysis. Thin foils for the transmission electron microscopy (TEM) were twin-jet electropolished in a solution consisting of 20 pct  $\text{HNO}_3$  and 80 pct methanol at  $-30$  °C. Desktop Microscopist DM2.2Net software (Lacuna Laboratories, Beaverton, OR) was used to analyze experimental selective area electron diffraction patterns (SAEDPs). The evolution of different phases during aging (*i.e.*, a relative increase or decrease in their volume fractions) was estimated from the relative intensities of the characteristic diffraction spots of these phases present on SAEDPs. The intensities of the diffraction spots from  $\text{Al}_3\text{Zr}$  and  $\text{Al}_3(\text{Sc,Zr})$  in the alloys without Sc and with Sc, respectively, were used as the references. This was possible because the particle number density and volume fractions of these phases did not change during aging. The mean size (diameter) and number density of particles were

**Table I. Compositions (Weight Percent) of the Alloys Studied in the Present Work**

Alloy ID	Zn	Mg	Cu	Mn	Zr	Sc	Si	Fe	Al
SSA000	7.14	2.30	1.61	0.27	0.17	0.00	0.09	0.12	bal
SSA018	7.17	2.20	1.58	0.30	0.18	0.18	0.09	0.13	bal
SSA038	7.11	2.14	1.56	0.25	0.17	0.38	0.09	0.09	bal
SSA048	7.05	2.35	1.55	0.27	0.14	0.49	0.09	0.10	bal

determined from dark-field TEM images using Clemex Vision Pro 3.5 image-processing software (Clemex Technologies Inc., Quebec, Canada). The foil thicknesses in the regions under consideration were measured using a contamination-spot-separation method.<sup>[30]</sup>

The Vickers microhardness was measured at a 500-g load in the regions of the flat, polished surfaces of the transverse cross sections, which were located near the mid-radius area of the DC-cast billet. Tensile specimens of the longitudinal orientation (parallel to the billet axis) were machined from cast billet sections located about 15 to 20 mm from the center of the billets. The specimen gage had a rectangular cross section that measured  $3.6 \times 2.5$  mm and a length of 20 mm. The longitudinal orientation was selected for study, because the Sc-free DC-cast alloy (SSA000) was found to have nil ductility in the transverse direction; the Sc-containing alloys, on the other hand, showed good ductility and isotropic tensile properties.<sup>[23]</sup> Thermal analyses of small pieces (approximately 10 to 15 mg) of heat-treated samples sealed in Al pans were conducted in a TA Instruments differential scanning calorimeter (New Castle, DE), model DSC Q1000, using a nitrogen atmosphere and a constant heating rate of 10 °C/min.

A two-step solution treatment was used in the microstructure analysis and tensile testing experiments, which consisted of holding the samples at 460 °C for 2 hours, heating to 480 °C, and holding at 480 °C for 1 hour. A one-step solution treatment was used in the differential scanning calorimetry (DSC) and microhardness testing experiments, which consisted of holding the samples at 460 °C for 48 hours. Every solution treatment was followed by water quenching. The aging of solution-treated samples was conducted by holding at (1) RT for up to 7680 hours, (2) 120 °C for up to 1270 hours, or (3) 150 °C for up to 72 hours. The artificial aging was conducted immediately after solution treatment and water quenching. Resistance-heated box furnaces with forced-air convection were used for heat treatment.

### III. RESULTS

#### A. TEM Analysis

##### 1. As-cast and solution-treated conditions

The TEM analysis of the alloys in the as-cast condition showed large particles containing Zn, Mg, and Cu located near grain boundaries. A dislocation network is formed, probably due to the internal stress relaxation during casting. In the alloys SSA038 and SSA048, primary  $\text{Al}_3(\text{Sc,Zr})$  particles with an  $\text{L1}_2$  cubic crystal structure are also present. These microstructure features are illustrated in Figure 1, for the alloy SSA038. No secondary  $\text{Al}_3(\text{Sc,Zr})$  particles are detected in this condition.

After solution treatment and water quenching, fine spherical secondary  $\text{Al}_3\text{Zr}$  and  $\text{Al}_3(\text{Sc,Zr})$  particles are detected in the Sc-free and Sc-containing alloys, respectively (Figure 2). Many regions in which these particles are detected are free of dislocations, which may indicate

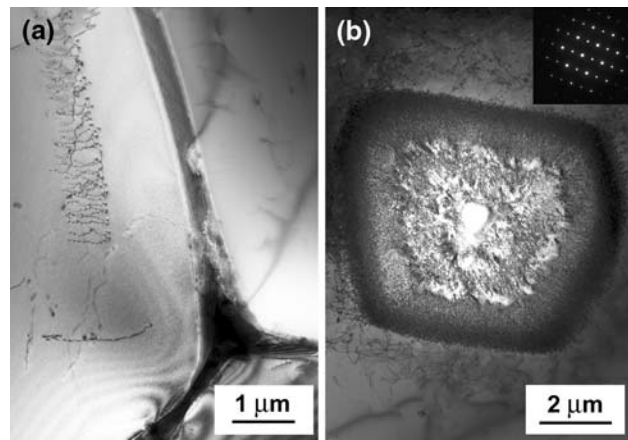


Fig. 1—TEM bright-field images of the microstructure of alloy SSA038 in as-cast condition. (a) An eutectic along the grain boundaries and a dislocation network. (b) A large primary  $\text{Al}_3(\text{Sc,Zr})$  particle identified by a SAEDP (insert) and energy-dispersive spectroscopy analysis.

homogeneous nucleation. The  $\text{Al}_3\text{Zr}$  particles formed in the SSA000 alloy during solution treatment are probably noncoherent or semicoherent with the matrix, because no elastic-strain-induced contrasts are detected near these particles (Figure 2(a)). The average size (diameter) of these particles is ~15 to 20 nm and the number density is  $\sim 5 \times 10^{14} \text{ cm}^{-3}$  (Figure 2(b)). On the other hand, a characteristic Ashby–Brown (AB) strain contrast can be seen around the secondary  $\text{Al}_3(\text{Sc,Zr})$  particles in the Sc-containing alloys in bright-field images under the Bragg conditions (Figure 2(c)), which indicates that these particles are coherent with the matrix.<sup>[31]</sup> The size of the  $\text{Al}_3(\text{Sc,Zr})$  particles varies from 5 to 40 nm, and the average size is estimated to be ~15 nm in the alloy SSA018 and ~22 nm in the alloy SSA038. The number density of these particles is  $\sim 1 \times 10^{15}$  to  $3 \times 10^{15} \text{ cm}^{-3}$  (Figure 2(d)). The number density and the size of the  $\text{Al}_3\text{Zr}$  and  $\text{Al}_3(\text{Sc,Zr})$  particles remain unchanged during the aging process described here. Larger particles of different phases, containing Fe, Mn, Mg, and Si, are also detected in the solutionized samples.

##### 2. Precipitation during natural aging

Characteristic patterns of diffuse spots associated with GP I zones are identified in the SAEDPs taken from the naturally aged samples (Figure 3). For example, rows of diffuse spots indexed as  $\{h,k,l\} = \{1,(2n+1)/4,0\}$  in the Al reciprocal lattice can be viewed in the  $\langle 001 \rangle_{\text{Al}}$  projections. The strongest diffuse spots from GP I are located at positions  $\{1,1/4,0\}_{\text{Al}}$  and  $\{1,7/4,0\}_{\text{Al}}$ , in agreement with previous works.<sup>[6,7,10]</sup> No GP II zones or  $\eta'$  particles were detected in the naturally aged samples. The diffraction spots at the positions  $\{100\}_{\text{Al}}$  and  $\{110\}_{\text{Al}}$  are from the  $\text{Al}_3\text{Zr}$  (SSA000 alloy) and  $\text{Al}_3(\text{Sc,Zr})$  (Sc-containing alloys) particles. The  $\text{Al}_3(\text{Sc,Zr})$  diffraction spots are much more intense than the  $\text{Al}_3\text{Zr}$  spots (Figure 3), due to a higher volume fraction of the  $\text{Al}_3(\text{Sc,Zr})$ .



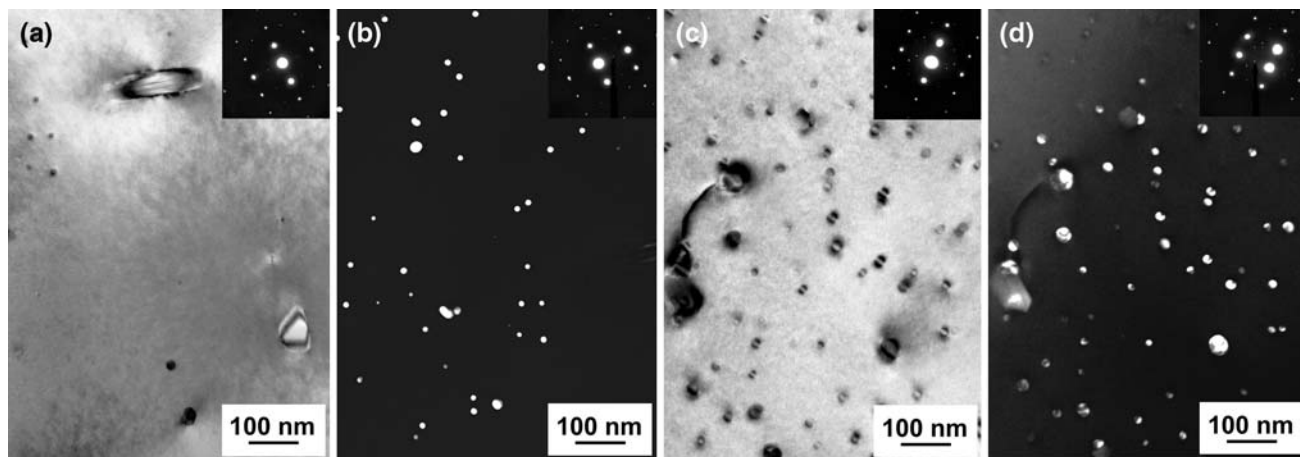


Fig. 2—TEM images of DC-cast alloys (a) and (b) SSA000 and (c) and (d) SSA038, after solution treatment and water quenching. (a) and (c) Bright-field images of areas with particles in  $\langle 112 \rangle_{\text{Al}}$  projection. (c) and (d) Dark-field images in  $\text{Al}_3\text{Zr}$  and  $\text{Al}_3(\text{Sc,Zr})$  reflexes, respectively. Corresponding SAEDPs are given as the inserts.

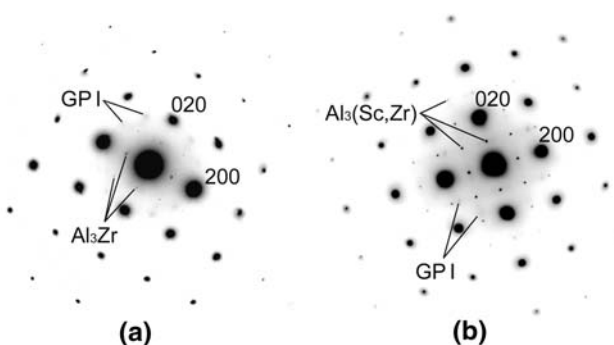


Fig. 3—SAEDPs in  $\langle 001 \rangle_{\text{Al}}$  projection of DC-cast alloys (a) SSA000 and (b) SSA038, after solution treatment, water quenching, and subsequent natural aging for  $\sim 1000$  h.

### 3. Precipitation during artificial aging at 120 °C

Typical SAEDPs of the samples after solution treatment, water quenching, and subsequent artificial aging at 120 °C for 24 hours are given in Figure 4. The diffuse spots associated with GP I zones are identified in the  $\langle 001 \rangle_{\text{Al}}$  projections (Figures 4(a) and (d)). These diffraction spots from GP I zones are more intense in the Sc-free sample. Additionally, diffuse spots from  $\eta'$  particles in the positions  $\{2/3, 2/3, 0\}_{\text{Al}}$ ,  $\{4/3, 4/3, 0\}_{\text{Al}}$ , and  $\{2/3, 4/3, 0\}_{\text{Al}}$  can be seen in the  $\langle 001 \rangle$  zone axes of the Sc-containing samples (Figure 4(d)). They are not seen in the sample without Sc (Figure 4(a)). Diffraction spots from GP II zones, in both SSA000 and SSA038 alloys, can be clearly identified in the  $\langle 111 \rangle_{\text{Al}}$  projection near the  $\{422\}/3_{\text{Al}}$  positions (Figures 4(b) and (e)) and in the  $\langle 112 \rangle_{\text{Al}}$  projection at  $\{311\}/2_{\text{Al}}$  positions (Figures 4(c) and (f)). Diffraction features from the  $\eta'$  phase particles can also be found in the  $\langle 111 \rangle_{\text{Al}}$  and  $\langle 112 \rangle_{\text{Al}}$  projections of both alloys. These are weak diffraction spots at  $1/3\{2\bar{2}0\}_{\text{Al}}$  and  $2/3\{2\bar{2}0\}_{\text{Al}}$  positions in the  $\langle 111 \rangle_{\text{Al}}$  projections (Figures 4(b) and (e)) and streaks parallel to  $\langle 11\bar{1} \rangle_{\text{Al}}$  at the  $1/3\{2\bar{2}0\}_{\text{Al}}$  and  $2/3\{2\bar{2}0\}_{\text{Al}}$  positions in  $\langle 112 \rangle_{\text{Al}}$  projections (Figures 4(c) and (f)).

In the  $\langle 112 \rangle_{\text{Al}}$  projection, GP I zones can also be identified as weak diffraction spots at  $1/3\{3\bar{1}\bar{1}\}_{\text{Al}}$  and  $2/3\{3\bar{1}\bar{1}\}_{\text{Al}}$ . This analysis indicates that the GP I and GP II zones and  $\eta'$  particles are present in both Sc-free and Sc-containing alloys after aging at 120 °C for 24 hours. Weaker intensities of the diffraction spots from GP I and stronger intensities of the diffraction spots from  $\eta'$  in the Sc-containing alloy are indications that the alloy without Sc contains a larger volume fraction of GP I and a lower volume fraction of  $\eta'$  than the Sc-containing alloy.

Dark-field images of the precipitate particles in the alloys with 0 and 0.38 pct Sc after aging for 24 hours are shown in Figures 4(g) and (h). These images were taken from a  $\eta'$  diffraction spot located at a  $2/3(2\bar{2}0)_{\text{Al}}$  position of the  $[112]$  zone axis. A higher volume fraction and a larger size of the  $\eta'$  particles in the Sc-containing alloy SSA038 than is found in the Sc-free SSA000 can be clearly recognized.

Figure 5 shows typical SAEDPs of the alloys without Sc and with 0.38 pct Sc, after aging at 120 °C for 162 hours. No diffraction spots from GP I zones are detected in this aged condition, indicating that these zones are completely dissolved. On the other hand, diffraction features of GP II zones and  $\eta'$  particles are observed in both alloys. In addition, the elongated spots at  $2/3\{220\}_{\text{Al}}$  and near  $\{220\}_{\text{Al}}$  (Figures 5(b) and (d)) are found, indicating the formation of equilibrium  $\eta$ -phase particles. Thus, 162-hour aging at 120 °C results in a similar precipitation structure, in the alloys both with and without Sc. Figures 5(g) and (d) illustrate dark-field images of the  $\eta'$  and  $\eta$  particles in the Sc-free and Sc-containing alloys, respectively, after aging at 120 °C for 162 hours. The mean particle size is approximately 8 nm; it is almost the same for the alloys with and without Sc, and is almost the same as in the Sc-containing alloy after aging for 24 hours. However, the number of elongated  $\eta'$  particles is considerably reduced in the samples aged longer (compare the TEM images in Figures 4 and 5).

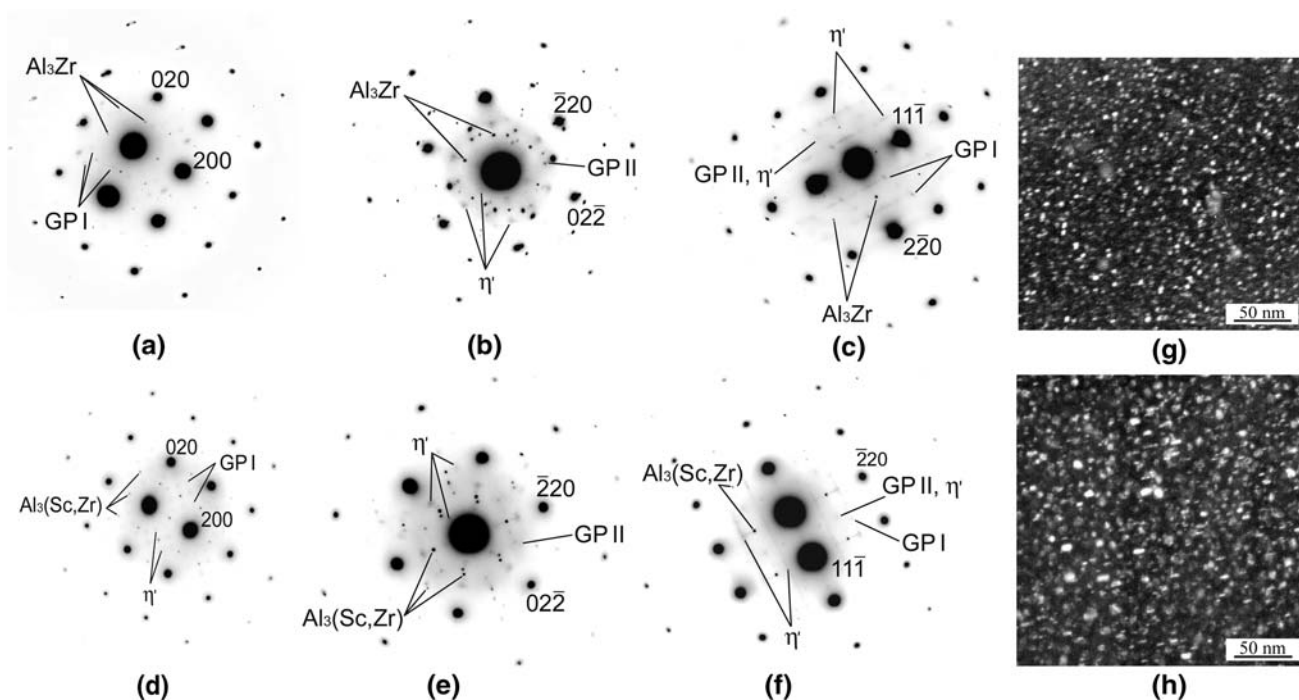


Fig. 4—SAEDPs in (a) and (d)  $\langle 001 \rangle_{\text{Al}}$ , (b) and (e)  $\langle 111 \rangle_{\text{Al}}$ , and (c) and (f)  $\langle 112 \rangle_{\text{Al}}$  projections. (g) and (h) Dark-field images of precipitates after aging at 120 °C for 24 h. The dark-field images were taken from  $\eta'$  spots located at  $2/3\{220\}_{\text{Al}}$  positions of a  $\langle 112 \rangle$  zone axis. DC-cast alloys (a), (b), (c), and (g) SSA000 and (d), (e), (f), and (h) SSA038.

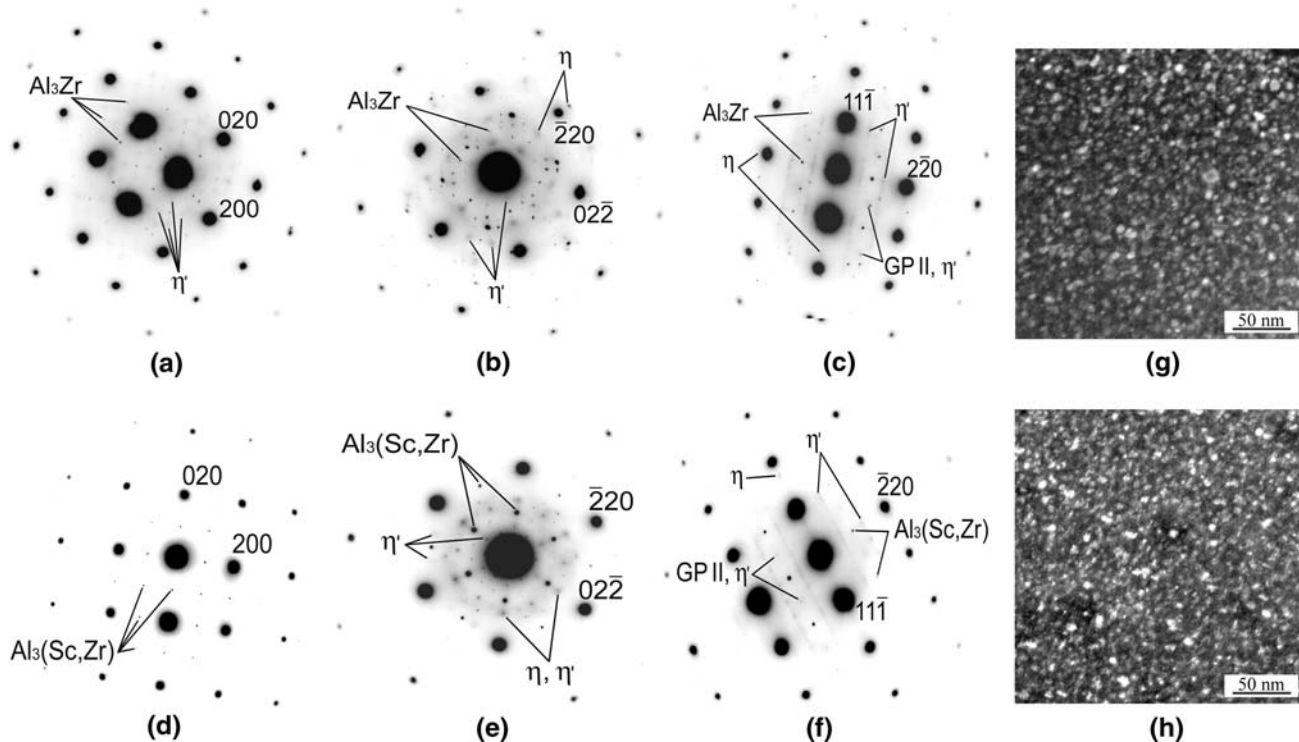


Fig. 5—SAEDPs in (a) and (d)  $\langle 001 \rangle_{\text{Al}}$ , (b) and (e)  $\langle 111 \rangle_{\text{Al}}$ , and (c) and (f)  $\langle 112 \rangle_{\text{Al}}$  projections. (g) and (h) Dark-field images of  $\eta'$  and  $\eta$  precipitates after aging at 120 °C for 162 h. (a), (b), (c), and (g) SSA000 and (d), (e), (f), and (h) SSA038.

#### 4. Precipitation during artificial aging at 150 °C

Typical SAEDPs of the alloys SSA000 and SSA038 after solution treatment, water quenching, and subse-

quent aging at 150 °C for 1 hour are given in Figure 6. Diffraction spots from GP I zones are absent; diffraction spots from  $\eta'$  particles are rather strong and can be easily

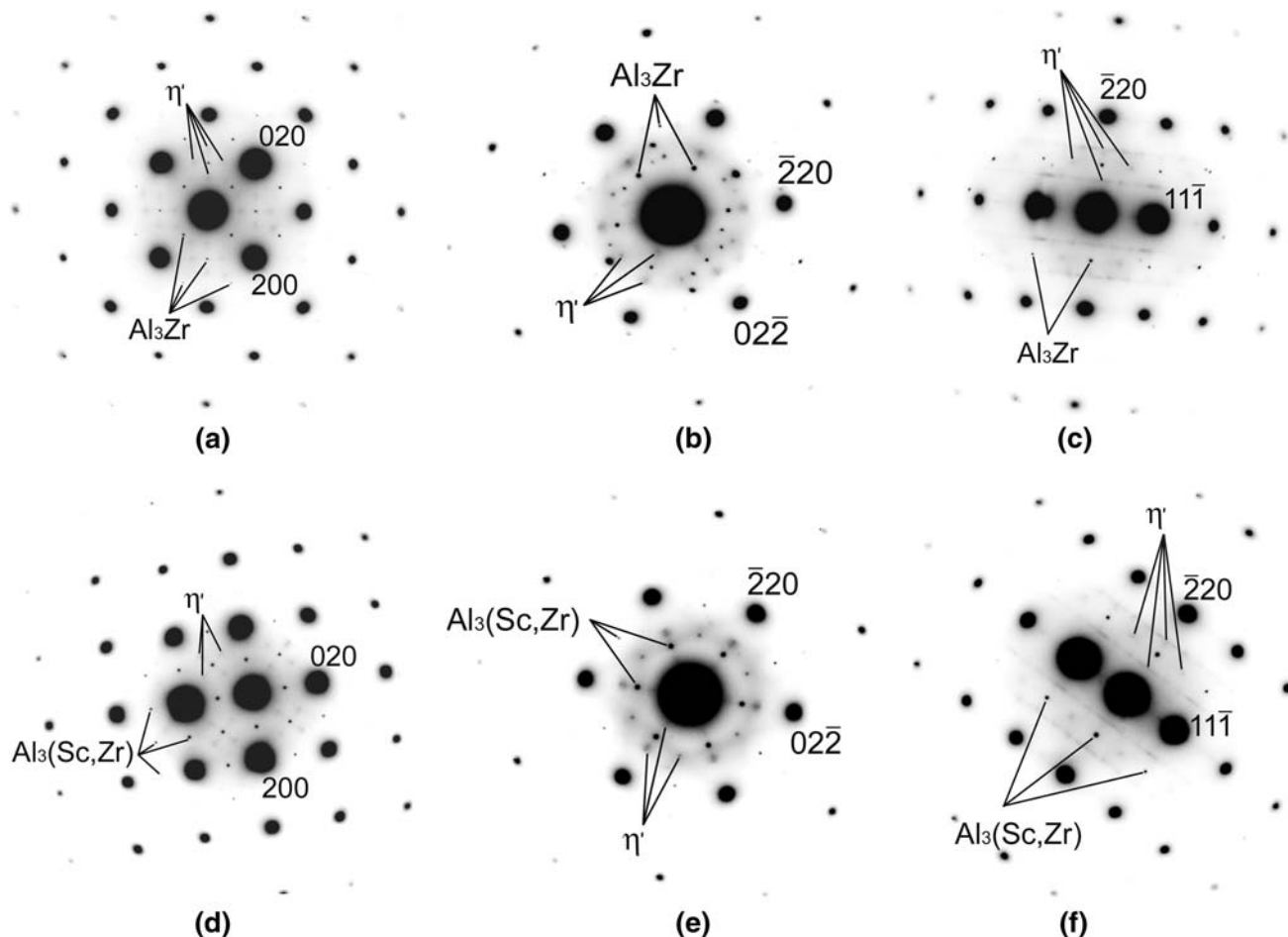


Fig. 6—SAEDPs in (a) and (d)  $\langle 001 \rangle_{\text{Al}}$ , (b) and (e)  $\langle 111 \rangle_{\text{Al}}$ , and (c) and (f)  $\langle 112 \rangle_{\text{Al}}$  projections of DC-cast alloys (a), (b), and (c) SSA000 and (d), (e), and (f) SSA038 after solution treatment, water quenching, and subsequent artificial aging at 150 °C for 1 h.

identified in all three diffraction zones. It is difficult to determine from these diffraction patterns whether GP II zones are still present in the alloys, because the diffraction features from GP II can be overshadowed by the  $\eta'$  diffraction (the diffraction spots from these precipitates are located very close to each other and the conclusive identification of GP II is possible only if the  $\eta'$  phase is absent or its volume fraction is very low). Figure 7 shows the SAEDPs of the alloys after artificial aging at 150 °C for 12 hours. Along with the diffraction features from  $\eta'$  particles, one can see the diffraction spots from the equilibrium  $\eta$  phase in the  $\langle 111 \rangle_{\text{Al}}$  and  $\langle 112 \rangle_{\text{Al}}$  projections (Figures 7(b), (c), (e), and (f)). After a 48-hour aging at 150 °C, the major precipitates identified with the use of SAEDPs are  $\eta'$  and  $\eta$  particles, in both the SSA000 and SSA038 alloys (Figure 8). However, elongated spots from the  $\eta$  in  $\langle 111 \rangle_{\text{Al}}$  projections become stronger (Figures 8(b) and (e)), suggesting that the volume fraction of the  $\eta$  phase increases significantly. Diffusive streaks along  $\{111\}_{\text{Al}}$  in  $\langle 112 \rangle_{\text{Al}}$  projections are thicker and more discrete, indicating coarsening of the  $\eta'$ -phase particles (Figures 8(c) and (f)).

Typical TEM images of the  $\eta'$  and  $\eta$  particles after aging at 150 °C for different periods of time are shown in Figure 9. Considerable growth of these particles at this

temperature is evident. After a 1-hour aging, the precipitates have the mean size of 2 to 3 nm, independent of the Sc content; however, their number density is slightly higher in the Sc-containing alloy (compare Figures 9(a) and (b)). After aging for 12 hours, the particle size increases to approximately 5 to 7 nm; the particles are slightly coarser in the Sc-containing alloy (Figures 9(c) and (e)). A dark-field image of preferentially  $\eta$  particles (Figure 9(d)) indicates that these particles are coarser (*i.e.*, their size is  $\sim 7$  to 8 nm) than the sum of both the  $\eta'$  and the  $\eta$  particles (compare Figures 9(c) and (d)). After a 48-hour aging, the mean size of the precipitates increases to  $\sim 11$  to 12 nm (Figure 9(f)); the size is slightly larger in the Sc-containing alloy. Thus, after any aging time at 150 °C, the precipitation character in both Sc-free and Sc-containing alloys is essentially the same, with the exception of a slightly coarser precipitate size in the Sc-containing alloys at the aging times longer than 1 hour.

## B. DSC Analysis of Aged Samples

### 1. Natural aging

During holding at RT of solution-treated samples, decomposition of the supersaturated solid solution



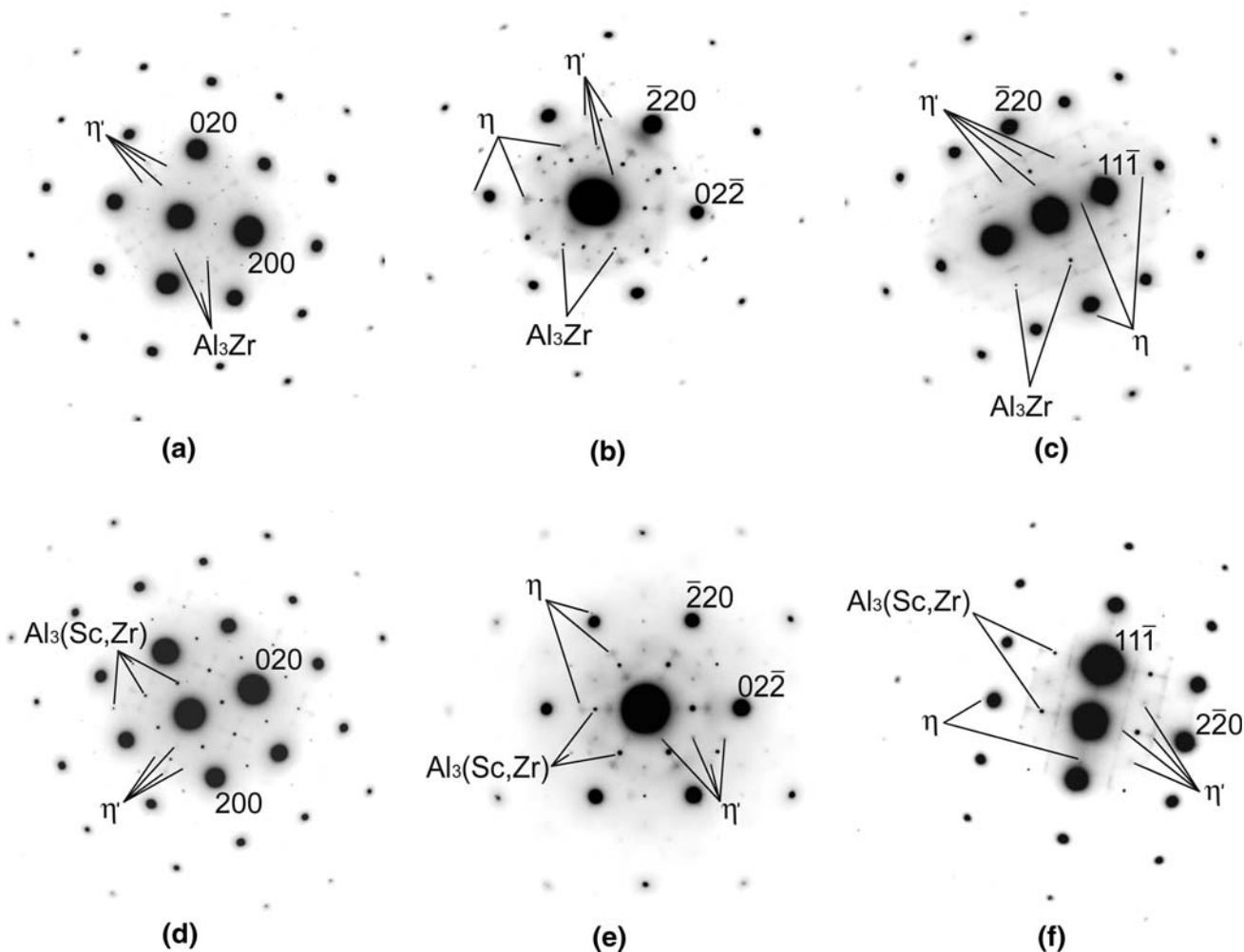


Fig. 7—SAEDPs of DC-cast alloys (a), (b), and (c) SSA000 and (d), (e), and (f) SSA038 after solution treatment (460 °C for 2 h and 480 °C for 1 h), water quenching, and subsequent artificial aging at 150 °C for 12 h.

occurs (natural aging), leading to the formation of GP I zones. Figure 10 shows DSC curves of the samples of the three alloys with different amounts of Sc that were solution treated and naturally aged for 7600 hours. Several superimposed endothermic and exothermic reaction peaks can be identified on the DSC curves. The endothermic reactions are due to the dissolution of the GP zones and the different phases during heating, while the exothermic reactions reflect the formation and growth of metastable and stable phases. This is in agreement with earlier reports.<sup>[11,32–37]</sup> Relative to the baseline (zero heat flow), five distinct regions can be identified.

Region I is characterized by an endothermic reaction between ~60 °C and 160 °C, with the maximum reaction rate at ~131 °C, which is due to the dissolution of the GP I zones. Region II is distinguished by an apparent exothermic reaction in the temperature range between 160 °C and 255 °C. The uneven shape of the exothermic signal in this region suggests the superposition of at least three exothermic reactions, with the reaction peaks located near 180 °C, 218 °C, and ~240 °C. The first exothermic reaction in this region is considered to be due to the

formation and growth of the  $\eta'$  particles, while the other two exothermic reactions are suggested to be a result of the formation of particles of the equilibrium  $\eta$  and  $T$  phases. This again is in agreement with earlier publications.<sup>[32–36]</sup> The presence of the  $T$  phase in these alloys in the equilibrium condition has been recently verified, through the thermodynamic assessment of the equilibrium phase diagrams using PANDAT\*\* software<sup>[38]</sup> and

---

\*\*PANDAT is a trademark of CompuTherm, LLC, Madison, WI

---

the X-ray diffraction of specimens annealed at 200 °C for 140 hours.<sup>[39]</sup>

Region III covers a wide temperature range, from 255 °C to ~450 °C, where a dominated endothermic reaction is overlapped by several exothermic reactions. The exothermic and endothermic reactions in this region are the results of the formation and dissolution of the equilibrium high-temperature phases. It is generally agreed that dissolution of the  $\eta$  and  $T$  phases contribute to the endothermic reaction in this region, while the



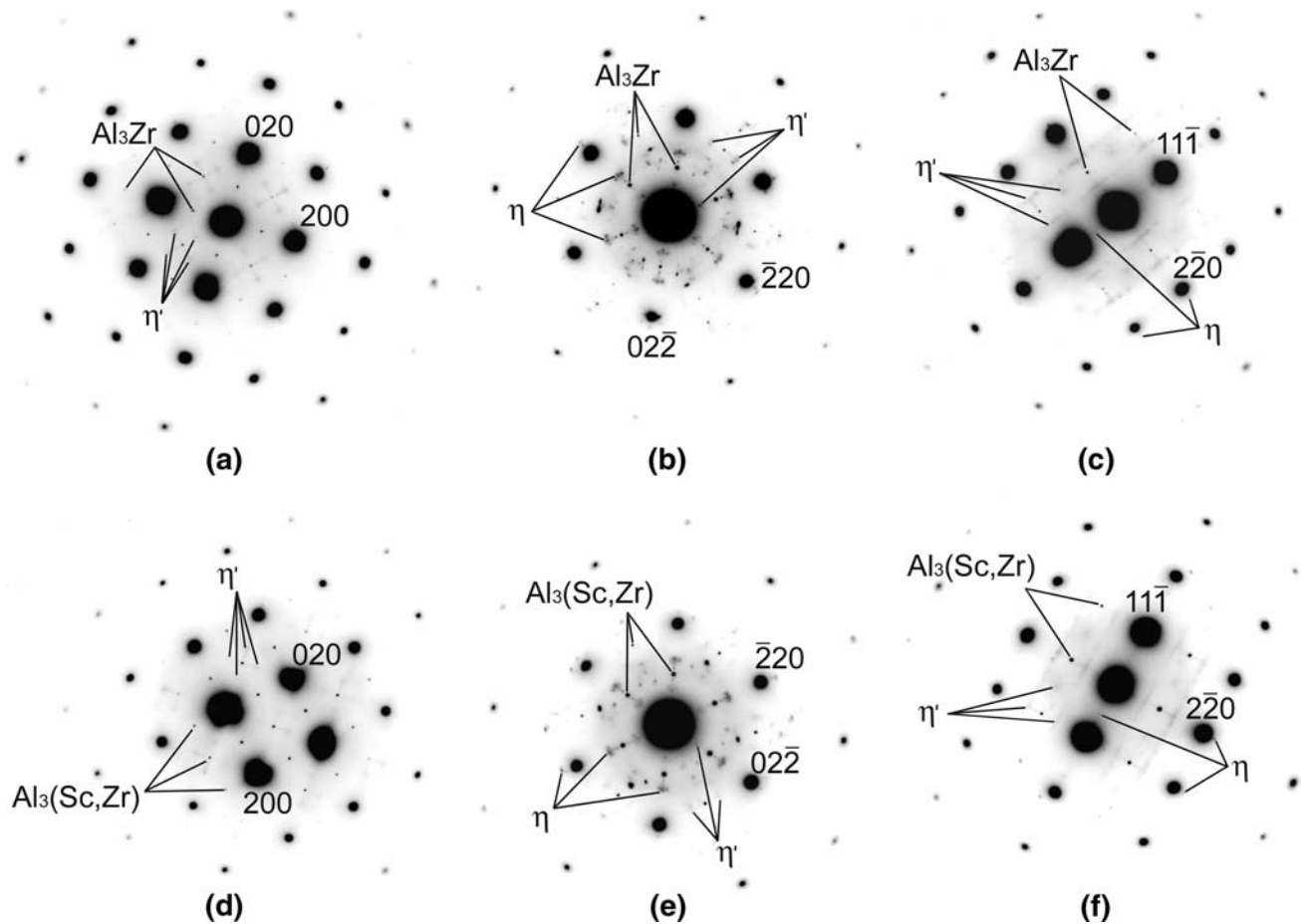


Fig. 8—SAEDPs in (a) and (d)  $\langle 001 \rangle_{\text{Al}}$ , (b) and (e)  $\langle 111 \rangle_{\text{Al}}$ , and (c) and (f)  $\langle 112 \rangle_{\text{Al}}$  projections of DC-cast alloys (a), (b), and (c) SSA000 and (d), (e), and (f) SSA038 after solution treatment, water quenching, and subsequent artificial aging at 150 °C for 48 h in (a) and (d)  $\langle 001 \rangle_{\text{Al}}$ , (b) and (e)  $\langle 111 \rangle_{\text{Al}}$ , and (c) and (f)  $\langle 112 \rangle_{\text{Al}}$  projections.

dissolution of the  $\eta'$  particles occurs in the temperature range of region II.<sup>[11,32–35]</sup> However, the endothermic reaction of the  $\eta'$  particle dissolution cannot be identified on the DSC scans from the naturally aged specimens, because of strong exothermic reactions caused by the formation and growth of the  $\eta$  and  $T$  phases (Figure 10). Region IV (450 °C to 520 °C) is associated with no reaction and corresponds to equilibrium solid solution; in region V (above 520 °C), equilibrium melting occurs.

The DSC analysis shows (Figure 10 and Table II) that the additions of Sc up to 0.38 pct do not change the positions of the peaks and intensities of the reactions in regions I and II; however, they slightly decrease the intensity of the endothermic reaction in region III (Table II). As the peak temperature of the endothermic reaction in region I is associated with the maximum rate of the precipitate dissolution and  $\Delta H_f$  is proportional to the volume fraction of the precipitates (or phases) and their molar heat of dissolution, one may conclude that the kinetics of the GP I zone formation, growth, and dissolution in the naturally aged Al-Zn-Mg-Cu alloy does not depend on the presence of Sc. Similarly, because the exothermic reactions in region II, which are

due to the formation and growth of the  $\eta'$ ,  $\eta$ , and  $T$  phases, are unaffected by Sc, one may conclude that the kinetics of these exothermic reactions during DSC heating of the naturally aged samples does not depend on the Sc content.

## 2. Artificial aging

The DSC patterns of the SSA-alloy samples with different amounts of Sc after solution treatment and artificial aging at 120 °C for 8 hours (underaged condition, Figure 15 (a)) are shown in Figure 11. Similar to the naturally aged condition, five regions with different heat flow responses can be identified on the DSC patterns (compare Figures 10 and 11). However, the endothermic region I is wider, because the upper temperature limit increases from 160 °C for the naturally aged samples to ~200 °C for the artificially aged samples, and the exothermic region II is now between 200 °C and 270 °C, with two clearly identified exothermic peaks, one at 220 °C and the other at ~245 °C. It is worth noting that, in the temperature range 75 °C to 160 °C, where dissolution of the GP I zones occurs in the naturally aged samples (Figure 10), the samples artificially aged for 8 hours show a relatively small

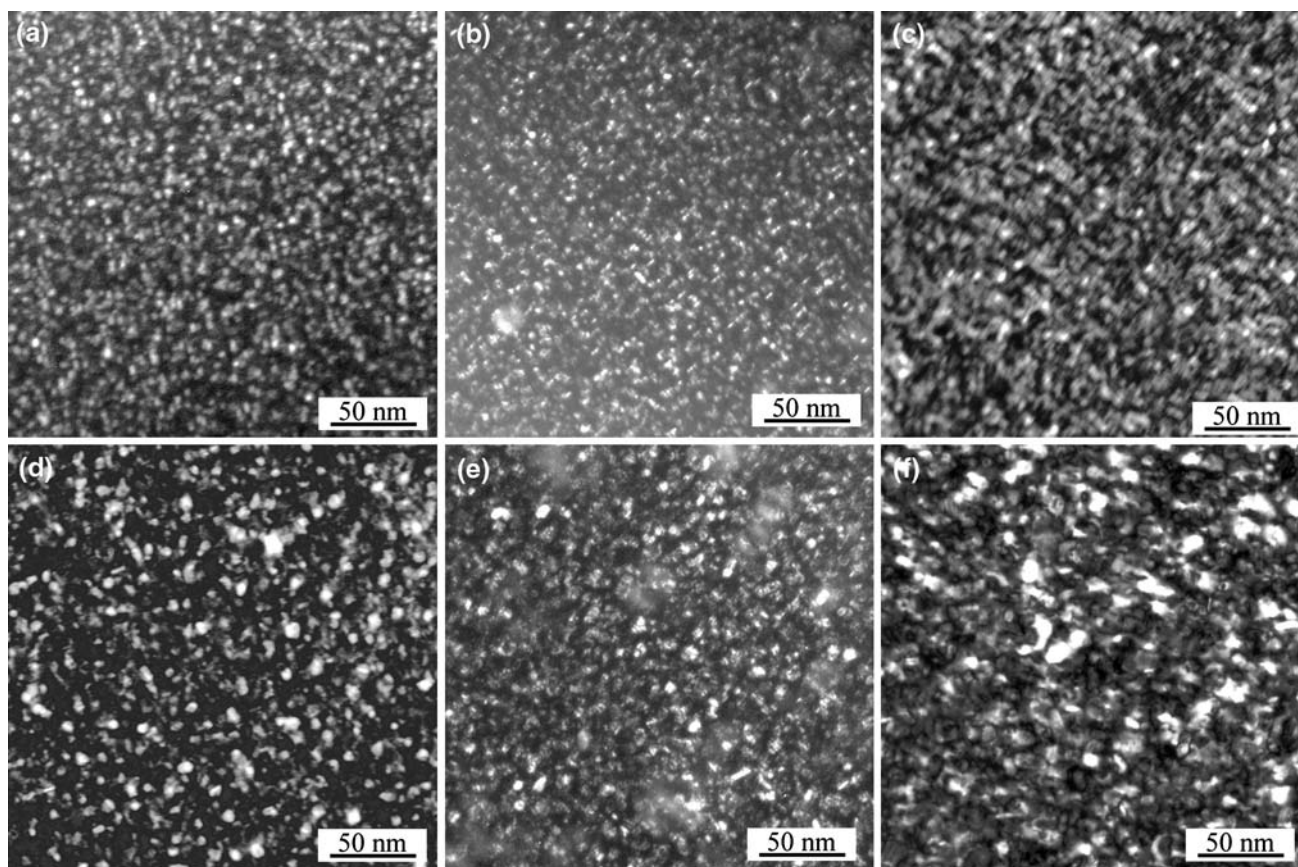


Fig. 9—TEM dark-field images of  $\eta'$  and  $\eta$  precipitates in the (a), (c), and (d) SSA000 and (b), (e), and (f) SSA038 alloys after aging at 150 °C for (a) and (b) 1 h, (c) through (e) 12 h, and (f) 48 h. The images (a), (b), (c), (e), and (f) were taken using closely located diffraction spots from  $\eta'$  and  $\eta$  phases, while image (d) was taken from an individual  $\eta$ -phase diffraction spot. In all cases, the beam direction was parallel to  $\langle 112 \rangle_{\text{Al}}$ .

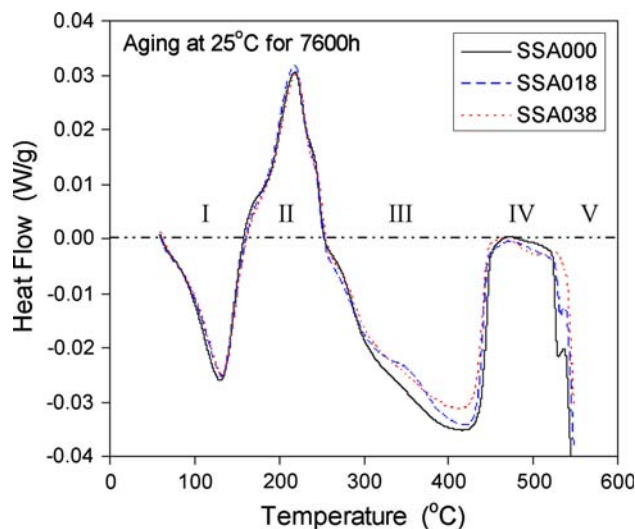


Fig. 10—(a) DSC thermographs of the DC-cast, solution-treated, water-quenched SSA-alloy samples naturally aged for 7600 h, with 0, 0.18, and 0.38 pct Sc. Characteristic five regions of different solid-state and liquid-solid reactions discussed in the text are outlined. Exothermic reactions are up. Heating rate is 10 °C/min.

decrease in heat flow (Figure 11). However, these artificially aged samples have the maximum rate of the endothermic reaction at a higher temperature of

~179 °C, which coincides with the first exothermic peak; the latter is related to the formation and growth of the  $\eta'$  particles in the naturally aged samples. This exothermic peak is not present in the 8-hour artificially aged samples. These observations suggest that the wider endothermic region I observed in the 8-hour artificially aged samples results from at least two superimposed processes: (1) the dissolution of the GP I zones in a lower temperature range and (2) the dissolution of the GP II zones and  $\eta'$  particles in a higher temperature range, with the peak reaction occurring at ~179 °C. The fact that the first reaction is weaker than the second one indicates a volume fraction of GP I lower than that of GP II and  $\eta'$  in these artificially aged samples. These results are in agreement with the recent work of Dupasquier *et al.*,<sup>[11]</sup> who also identified two distinct endothermic reactions in the temperature range of 100 °C to 250 °C for an Al-Zn-Mg alloy after different aging conditions. These authors used a combination of different characterization techniques, such as positron lifetime spectroscopy, coincidence Doppler broadening spectroscopy, small-angle X-ray scattering, and TEM, to analyze the processes responsible for these reactions. They came to a similar conclusion: that the lower temperature endothermic reaction was due to the dissolution of the GP I zones and the higher temperature endothermic reaction, which developed only after artificial aging, was due to the dissolution of the GP II

**Table II. Enthalpy,  $\Delta H$ , of the Reactions in Regions I, II, and III for Naturally Aged and Artificially Aged Alloys with Different Amounts of Sc**

Alloy	$\Delta H$ (J/g)		
	Region I Endotherm	Region II Exotherm	Region III Endotherm
Aged at 25 °C for 7600 h			
SSA000	-7.5	8.7	-28.6
SSA018	-7.0	9.1	-25.4
SSA038	-7.5	8.2	-24.4
Aged at 120 °C for 8 h			
SSA000	-5.8	5.0	-24.9
SSA018	-7.9	3.8	-26.6
SSA038	-7.4	4.1	-25.4
Aged at 120 °C for 162 h			
SSA000	-4.7	1.1	-28.7
SSA018	-5.6	0.8	-29.0
SSA038	-5.1	0.4	-28.2

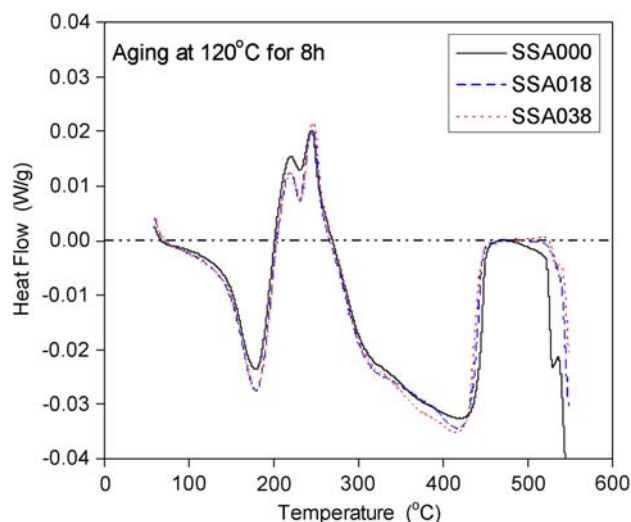


Fig. 11—DSC traces of DC-cast SSA-alloy samples with different amounts of Sc after solution treatment, water quenching, and aging at 120 °C for 8 h (underaging). Exothermic reactions are up. Heating rate is 10 °C/min.

zones. However, we suggest that the dissolution of  $\eta'$  is also responsible for the second endothermic reaction, because the exothermic peak from the formation and growth of the  $\eta'$  particles is not present on the DSC scans from the artificially aged samples (compare Figures 10 and 11).

The temperature positions of the two exothermic reactions in region II for the 8-hour artificially aged samples (Figure 11) are close to the positions of the second and third exothermic reactions in the naturally aged samples (Figure 10). Therefore, similar to the naturally aged samples, these exothermic reactions are probably also due to the formation and growth of the particles of the equilibrium  $\eta$  and  $T$  phases.<sup>[35–37]</sup> The reactions in regions III, IV, and V for the artificially aged samples involve equilibrium phases, and the patterns are similar to those for the naturally aged

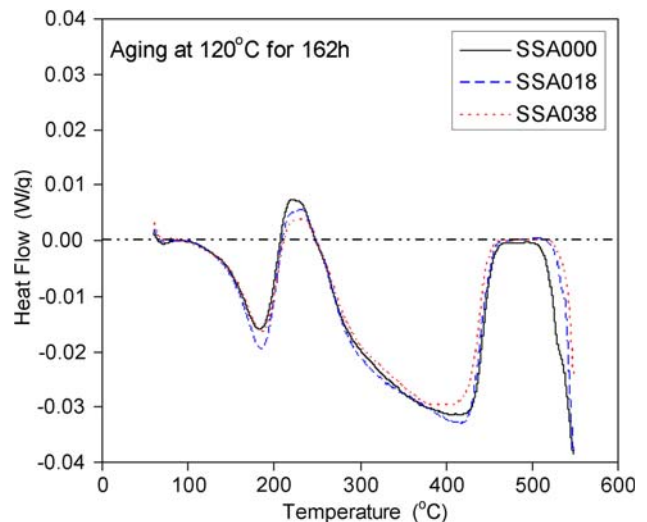


Fig. 12—DSC traces of DC-cast SSA-alloy samples with different amounts of Sc after solution treatment, water quenching, and aging at 120 °C for 162 h (peak aging). Exothermic reactions are up. Heating rate is 10 °C/min.

samples. The enthalpies of reactions in regions I, II, and III are given in Table II. An increase in the amount of Sc from 0 to up to 0.38 pct does not change the positions of the reaction peaks; however, the absolute values of the enthalpy of the endothermic reaction in region I increases by about 25 pct, and the enthalpy of the exothermic reaction in region II decreased by about 18 pct. These results indicate that higher volume fractions of the GP II zones and  $\eta'$  phase are present in the Sc-containing alloys than in the alloy without Sc, and that, probably, some amount of  $\eta$  phase is also present in the Sc-containing alloys after the 8-hour artificial aging.

Figure 12 shows the DSC patterns of the samples after solution treatment and aging at 120 °C for 162 hours (peak-aged condition, Figure 15(a)). No reaction due to the GP I zone dissolution can be identified in the low-temperature range of the endothermic region I, which indicates that, if GP I zones are present in this aging condition, their volume fraction must be very low. This is supported by TEM analysis, which was also not able to identify GP I zones after the 162-hour aging (Figure 5). The first endothermic peak occurs at 183 °C in the alloy without Sc and at 185 °C to 186 °C in the alloys with 0.18 and 0.38 pct Sc. Instead of two exothermic reactions (at ~220 °C and 245 °C) seen in the samples aged for 8 hours (Figure 11), only one exothermic reaction (at ~227 °C) occurs in the 162-hour aged samples in region II, and the apparent enthalpy of the reaction is rather low, at 1.1 J/g for the Sc-free sample and 0.4 J/g for the sample containing 0.38 pct Sc (Table II). Such behavior indicates that the peak-aged samples contain both metastable  $\eta'$  and stable  $\eta$  (and possibly  $T$ ) particles, which leads to the reduction of the exothermic reaction of formation of these particles. An increase in the amount of Sc from 0 to 0.38 pct slightly increases the absolute value of the enthalpy of reaction in region I (Table II) and decreases the enthalpy of



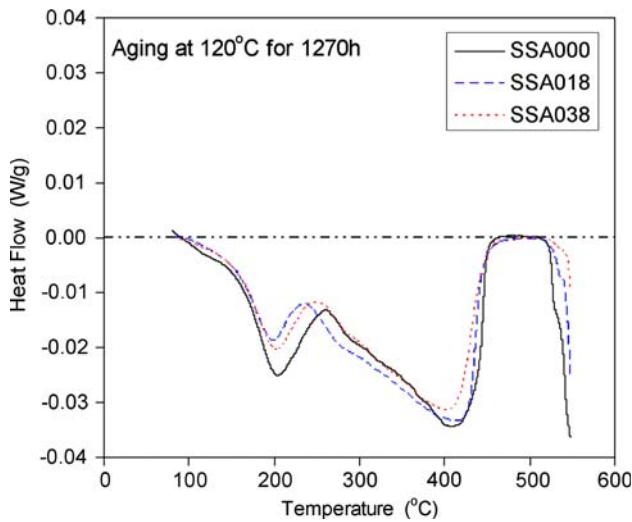


Fig. 13—DSC traces of DC-cast SSA-alloy samples with different amounts of Sc after solution treatment, water quenching, and aging at 120 °C for 1270 h (overaging). Exothermic reactions are up. Heating rate is 10 °C/min.

reaction in region II. Both results may indicate that the Sc-containing alloys contain a slightly higher volume fraction of the metastable and stable phases than does the Sc-free alloy.

Figure 13 illustrates the DSC curves of the alloy samples after aging for 1270 hours at 120 °C (overaged condition, Figure 15(a)). An overall endothermic response can be seen during the heating of the samples up to the solid-solution solvus temperature (445 °C to 450 °C), although additional superimposed endothermic and exothermic reactions can also be identified in the temperature range 150 °C to 300 °C. The endothermic reaction has a maximum near 200 °C; the exothermic reaction has a maximum at a temperature of 261 °C for 0 pct Sc and ~245 °C for 0.38 pct Sc. The endothermic reaction near 200 °C is more intense in the alloy without Sc, which may indicate that this alloy has a higher volume fraction of the metastable phases, which dissolve in this temperature range.

### C. Effect of Sc on Microhardness after Natural and Artificial Aging

#### 1. Natural aging

Figure 14 shows the effect of aging time at RT on the Vickers microhardness,  $H_V$ , of three alloys, SSA000, SSA018, and SSA038, which were initially solution treated at 460 °C for 48 hours and water quenched. About 10 minutes after water quenching, the  $H_V$  is 0.85 GPa for the alloy without Sc, 0.91 GPa for the alloy with 0.18 pct Sc, and 0.98 GPa for the alloy with 0.38 pct Sc. The microhardness increases logarithmically with an increase in the aging time, due to the formation and growth of GP I zones. Three regions with different rates of microhardness increase can be easily identified. A slow increase in the microhardness during the first few minutes after solution treatment (region A in Figure 14) reflects an incubation period, which is

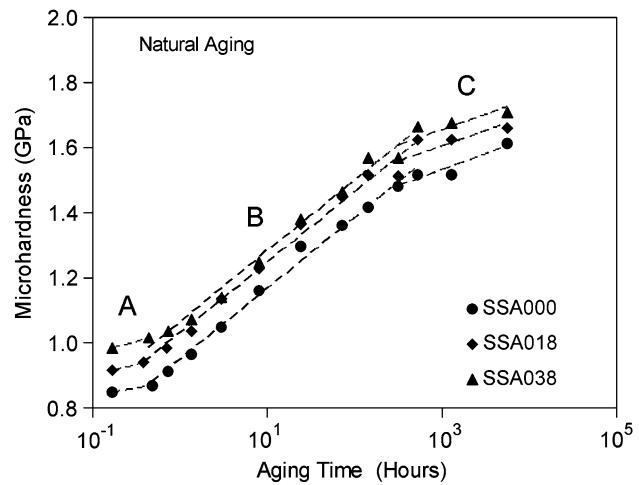


Fig. 14—RT Vickers microhardness of DC-cast alloys SSA000, SSA018, and SSA038 after solution treatment, water quenching, and natural aging for different periods of time.

Table III. Values of Parameters  $a$  and  $b$  (Equation [1]) for Regions B and C of Natural Aging (Figure 14)

Alloy	Region B		Region C	
	$a$ (MPa)	$b$ (MPa)	$a$ (MPa)	$b$ (MPa)
SSA000	94.6	948	42.8	1234
SSA018	93.9	1029	41.0	1320
SSA038	94.0	1064	40.9	1370

required for the solute elements to diffuse short distances, in order to nucleate the GP I zones. The nucleation and growth of the GP I zones leads to a rapid increase in the microhardness in region B, which is within a time frame of ~30 minutes to 600 hours. At longer aging times, above 600 hours (region C), the rate of the microhardness increase slows, which is probably due to the precipitate coarsening at a near-saturated volume fraction of the GP zones. The “equilibration” of the chemical composition of GP I at longer holding times<sup>[11]</sup> may also contribute to this effect.

There is no effect of Sc on the microhardness increase during natural aging (Figure 14). Every 0.1 pct added Sc increases the microhardness by about 30 to 40 MPa, and this increase does not depend on the natural aging time. The dependence of  $H_V$  on the aging time can be described by a logarithmic relationship:

$$H_V = a \ln(t) + b \quad [1]$$

where  $t$  is the aging time (in hours) and the parameters  $a$  and  $b$  for regions B and C are given in Table III.

#### 2. Artificial aging

Figure 15 illustrates the RT microhardness of the DC-cast alloys SSA000, SSA018, and SSA038 after solution treatment and artificial aging at 120 °C and 150 °C for different time periods. For these alloys, the peak microhardness occurs after about 162 and 12 hours of aging at 120 °C and 150 °C, respectively.



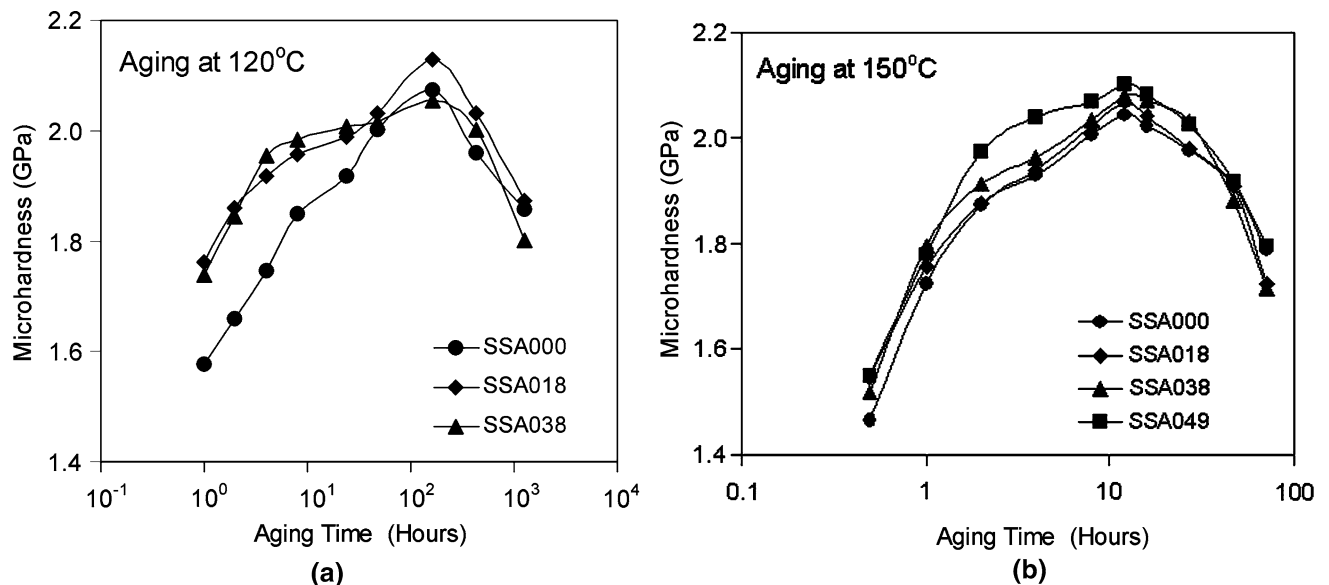


Fig. 15—RT Vickers microhardness of the DC-cast alloys SSA000, SSA018, SSA038, and SSA048 after solution treatment, water quenching, and artificial aging at (a) 120 °C and (b) 150 °C, for different periods of time.

The peak positions do not depend on the amount of Sc in the alloys. An increase in the aging time beyond the peak leads to a rapid decrease in the microhardness.

During aging at 120 °C, the maximum effect on the microhardness from the Sc addition occurs after about 1 to 8 hours of aging (Figure 15(a)). In this aging condition, the microhardness of the alloy with 0.18 pct Sc is about 180 to 200 MPa higher than that of the alloy without Sc. The alloys with 0.18 and 0.38 pct Sc have almost the same microhardness values. The dependence of the microhardness on the logarithm of aging time at  $t < 8$  hours and  $T = 120$  °C is steeper for the Sc-containing alloys; for example  $dHv/d(\ln t) \approx 110$  and  $\sim 155$  MPa for SSA000 and SSA038, respectively (Figure 15(a)). However, above  $\sim 8$  hours of aging, the increase in microhardness slows considerably in the Sc-containing alloys. The decrease in the microhardness difference between the Sc-containing and Sc-free alloys in the peak-aged condition may be attributed to larger number of  $\eta$  particles in the Sc-containing alloys. After peak aging, the microhardness of all three alloys is almost the same, within  $\pm 2$  pct of the standard error.

During aging at 150 °C, the maximum increase in microhardness due to the presence of Sc is observed after 0.5 to 4 hours of aging (Figure 15(b)). The increase in the Sc content shifts this maximum toward longer aging times. The microhardness of the alloy with 0.18 pct Sc is about 80 MPa higher than that for the alloy without Sc, after  $\sim 0.5$  hour aging, while the maximum difference in the microhardness of the SSA048 and SSA000 alloys of  $\sim 110$  MPa is achieved after a  $\sim 4$ -hour aging. At longer aging times, the increase in microhardness in the Sc-containing alloys slows. In the peak-aged condition (12 hours at 150 °C), the microhardness of all four alloys is almost the same,  $\sim 2.04$  to  $2.10$  GPa. An increase in the aging time beyond 12 hours leads to a decrease in the microhardness. After 48 hours, the microhardness is within the range of

1.88 to 1.92 GPa, regardless of the amount of Sc (Figure 15(b)).

#### D. Effect of Sc and Heat Treatment on Deformation Behavior of Cast Al-Zn-Mg-Cu Alloys

Figures 16 through 18 illustrate the RT deformation behavior of the DC-cast alloys with different amounts of Sc after various aging conditions. The average tensile properties corresponding to these conditions are tabulated in Tables IV through VI. The alloy specimens were solution treated by holding at 460 °C for 2 hours, heating to 480 °C, and holding at 480 °C for an additional 1 hour, and then water quenched prior to aging. Aging was conducted at (1) RT for 0.2 and 192 hours (Figure 16); (2) 120 °C for 8, 24, 162, and 720 hours (Figure 17); and (3) 150 °C for 1, 6, 12, and 48 hours (Figure 18).

##### 1. Natural aging

In a freshly quenched condition, *i.e.*, after solution treatment, water quenching, and a 0.2-hour holding at RT (Figure 16(a)), the alloys have the lowest strengths and the highest ductility values. The yield strength (YS) and ultimate tensile strength (UTS) increase, from 155 to 224 MPa and from 305 to 410 MPa, respectively, and the plastic strain (El) decreases, from 27 to 17 pct, with an increase in the Sc content from 0 to 0.49 pct (Table IV). The strengths of the alloys increase with an increase in the RT aging time (Figure 16 and Table IV). However, the increment is higher in the Sc-containing alloys than in the alloy without Sc. For example, after 192 hours of natural aging, YS = 285 MPa in alloy SSA000, which is about 130 MPa higher than in the freshly quenched condition. At the same time, the 192-hour natural aging increases the YS values of the Sc-containing alloys SSA018 and SSA038 by about 170 and 150 MPa, respectively. The major

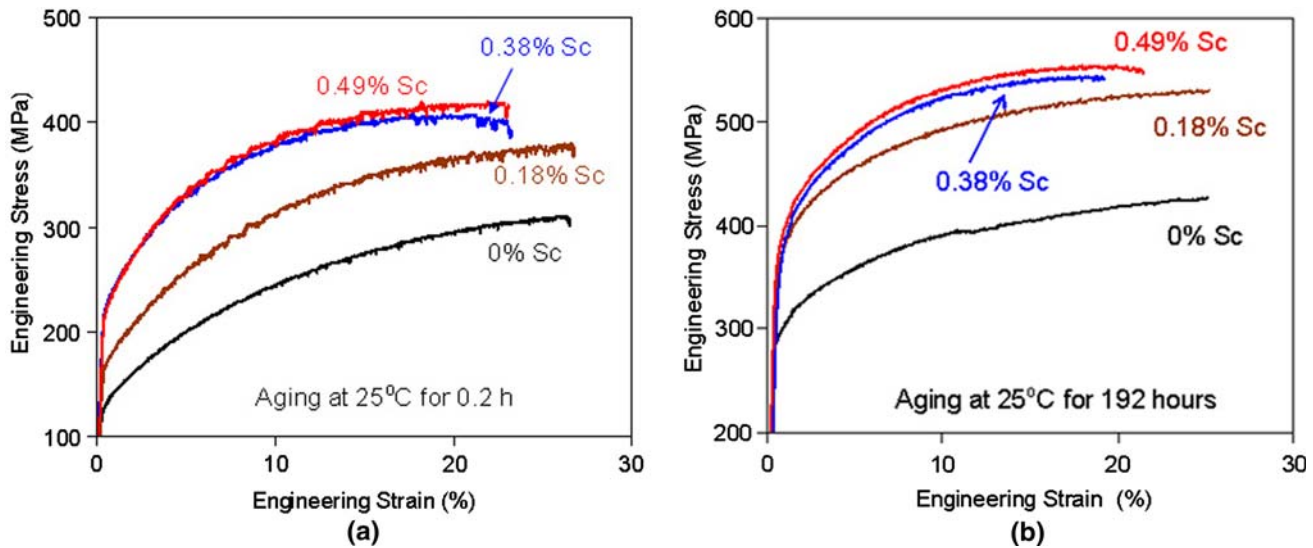


Fig. 16—RT stress-strain curves of DC-cast alloys SSA000, SSA018, SSA038, and SSA048 after solution treatment, water quenching, and natural aging for (a) 0.2 and (b) 192 h.

increase in the YS and UTS occurs with an increase in Sc from 0 to 0.18 pct. Only a very slight increase in the YS and UTS occurs in the range of 0.38 to 0.49 pct Sc.

### 2. Artificial aging at 120 °C

Deformation curves of the alloys with different amounts of Sc after artificial aging at 120 °C for different periods of time are shown in Figures 17(a) through (d), and the properties are tabulated in Table V. After aging for 8 hours at 120 °C, both the YS and the UTS increase considerably relative to the as-solution-treated condition (compare Figures 17(a) and 16(a)). For example, an increase in YS by 302 MPa and in UTS by 220 MPa occurs in the alloy SSA000, which does not contain Sc. An increase in the strength values due to Sc is almost the same as in the as-solution-treated alloys, that is,  $\Delta YS \approx 65$  MPa and  $\Delta UTS \approx 74$  to 78 MPa for SSA038, relative to the properties of SSA000. A further increase in the aging time to 162 hours (this corresponds to the peak aging condition, Figure 15(a)), leads to the achievement of the maximum strength values in these cast alloys; however, ductility sharply decreases, especially in the alloy without Sc (Table V). During the aging time frame from 8 to 162 hours, an increase in the strength values due to Sc is almost the same as in the as-solution-treated alloys; for example, the YS and UTS of SSA038 are about 65 and 78 MPa higher than those of SSA000. However, during longer aging times, in an overaged condition (720 hours at 120 °C), the contribution from Sc to the strength values decreases very dramatically, by about 30 to 50 pct, and the YS of SSA038 is only 37 MPa higher than that of SSA000 (Table V).

### 3. Artificial aging at 150 °C

The stress-strain curves of the alloys with different amounts of Sc after artificial aging at 150 °C for different periods of time are given in Figures 18(a)

through (d), and the properties are tabulated in Table VI. The strength of the alloys after a 1-hour aging at 150 °C is almost the same as after an 8-hour aging at 120 °C (compare Figures 18(a) and 17(a)). As compared to aging at 120 °C, a shorter aging time (6 to 12 hours at 150 °C vs. ~162 hours at 120 °C) is required to achieve the peak-aging condition, which provides the highest strength in these alloys. An additional increase in the aging time at 150 °C to 48 hours (overaging, Figure 18(d) and Table VI) results in a decrease in the YS by 25 to 33 MPa and in the UTS by 18 to 24 MPa, as compared to the properties in the peak-aging condition.

An increase in the Sc content from 0 to 0.38 pct results in a substantial increase in both YS and UTS; in the range of 0.38 to 0.49 pct Sc, on the other hand, only a slight increase in strength is observed (Figure 18 and Table VI). After aging at 150 °C for 1 hour, the YS of the alloy SSA038 is about 79 MPa higher than that of the SSA000 (Table VI). After a 6-hour aging, this difference is 48 MPa; after 12 hours, it decreases to 21 to 29 MPa. It should be noted that the maximum tensile strength of the Sc-containing alloys (~614 MPa) is achieved after a 6-hour aging, while the maximum strength of the alloy without Sc (~553 MPa) is achieved after a 12-hour aging at this temperature. This is additional evidence that Sc accelerates the artificial aging of this 7000-series alloy.

## IV. DISCUSSION

The results of the present work show that the presence of Sc in amounts from 0.18 to 0.49 pct in the Al-Zn-Mg-Cu DC-cast alloy does not have any effect on the aging kinetics at RT. On the other hand, a considerable increase in the microhardness due to the Sc addition is observed at the early stages of aging at 120 °C (at aging times from 1 to up to 8 hours); at longer aging times,

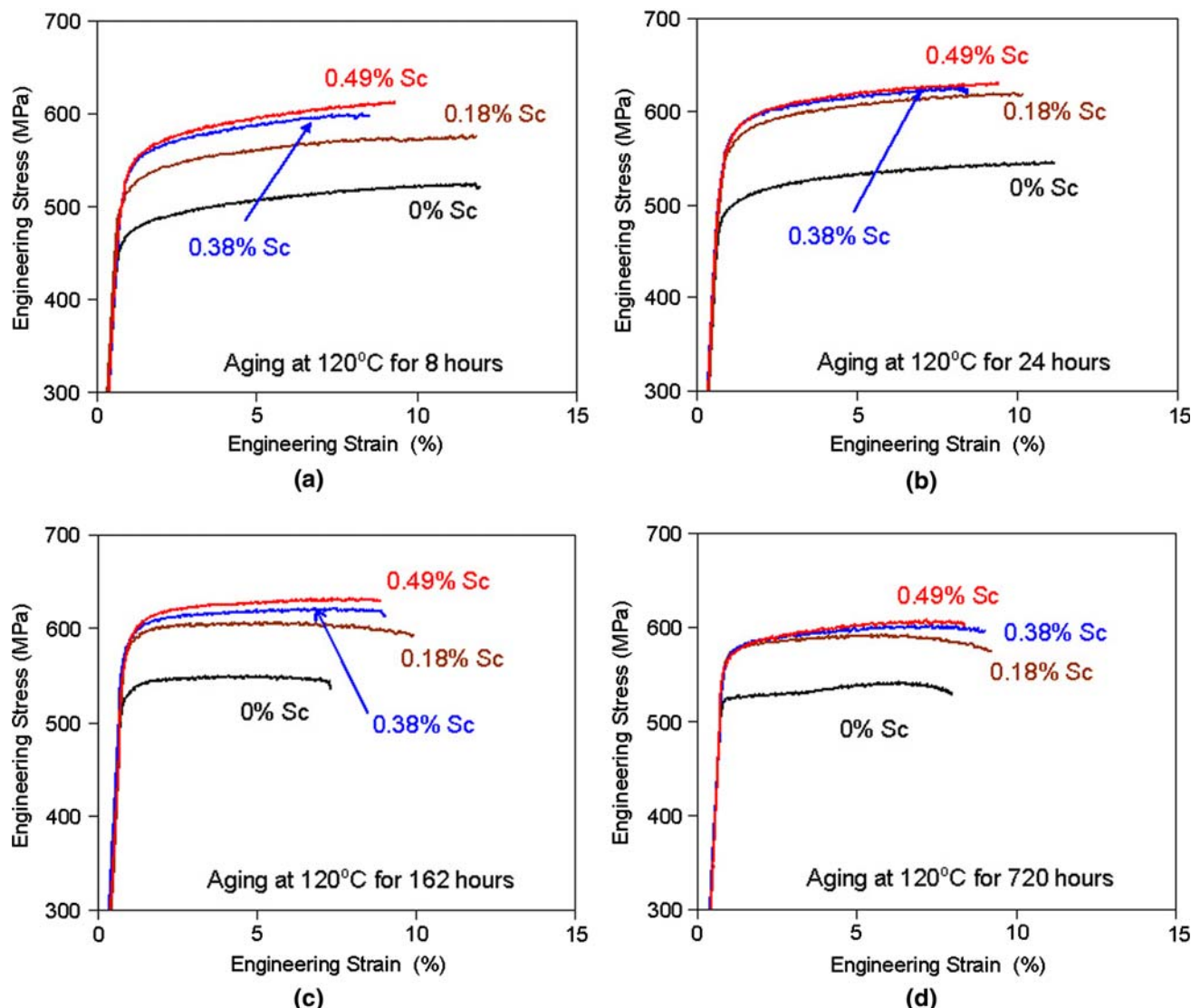


Fig. 17—RT stress-strain curves of DC-cast alloys SSA000, SSA018, SSA038, and SSA048 after solution treatment and aging at 120 °C for (a) 8, (b) 24, (c) 162, and (d) 720 h.

however, the aging response of the Sc-containing alloys slows. In the peak-aged condition, the difference in the microhardness of the alloys with and without Sc becomes minimal. A similar, but less pronounced, effect of Sc on the microhardness of these alloys is found during aging at 150 °C. The maximum effect from the Sc addition on the microhardness is observed after ~0.5 to 4 hours of aging at 150 °C. At longer aging times, the increase in the microhardness in the Sc-containing alloys slows. The results of the tensile tests also indicate that Sc accelerates the aging process at 150 °C by providing maximum tensile strength after aging for 6 hours; in the alloy without Sc, however, the maximum tensile strength is achieved after a 12-hour aging. We will make an attempt to explain these effects of Sc on the aging process and the mechanical properties of the Al-Zn-Mg-Cu alloy.

First, it is necessary to point out that all of the alloys studied also contain ~0.17 pct Zr. After DC casting, all of the Sc and Zr are present in the supersaturated solid

solution in the SSA000 and SSA018 alloys; however, some of the Sc and Zr are present in the form of primary  $\text{Al}_3(\text{Sc,Zr})$  particles in the SSA038 and SSA048 alloys.<sup>[20]</sup> During the solution treatment of these alloys, which followed after the DC casting, these supersaturated solutes precipitate into fine spherical particles with an  $\text{L}_{12}$  cubic structure. In the Sc-containing alloys, this precipitation results in coherent  $\text{Al}_3(\text{Sc,Zr})$  particles (the particle coherency was identified by the presence of the Ashby–Brown contrast), with a particle size of about 15 to 20 nm and a number density of  $\sim 1$  to  $3 \times 10^{15} \text{ cm}^{-3}$ . The number density slightly increases with an increase in the Sc content. In contrast to this situation, fine metastable  $\text{Al}_3\text{Zr}$  particles (also with the  $\text{L}_{12}$  ordered cubic structure) formed in the Sc-free SSA000 alloy. These  $\text{Al}_3\text{Zr}$  particles do not produce the Ashby–Brown contrast, which may indicate that these are semicoherent or noncoherent particles. The number density of the  $\text{Al}_3\text{Zr}$  particles is much smaller, only  $\sim 5 \times 10^{14} \text{ cm}^{-3}$ , and their size is about 15 nm. These particles probably

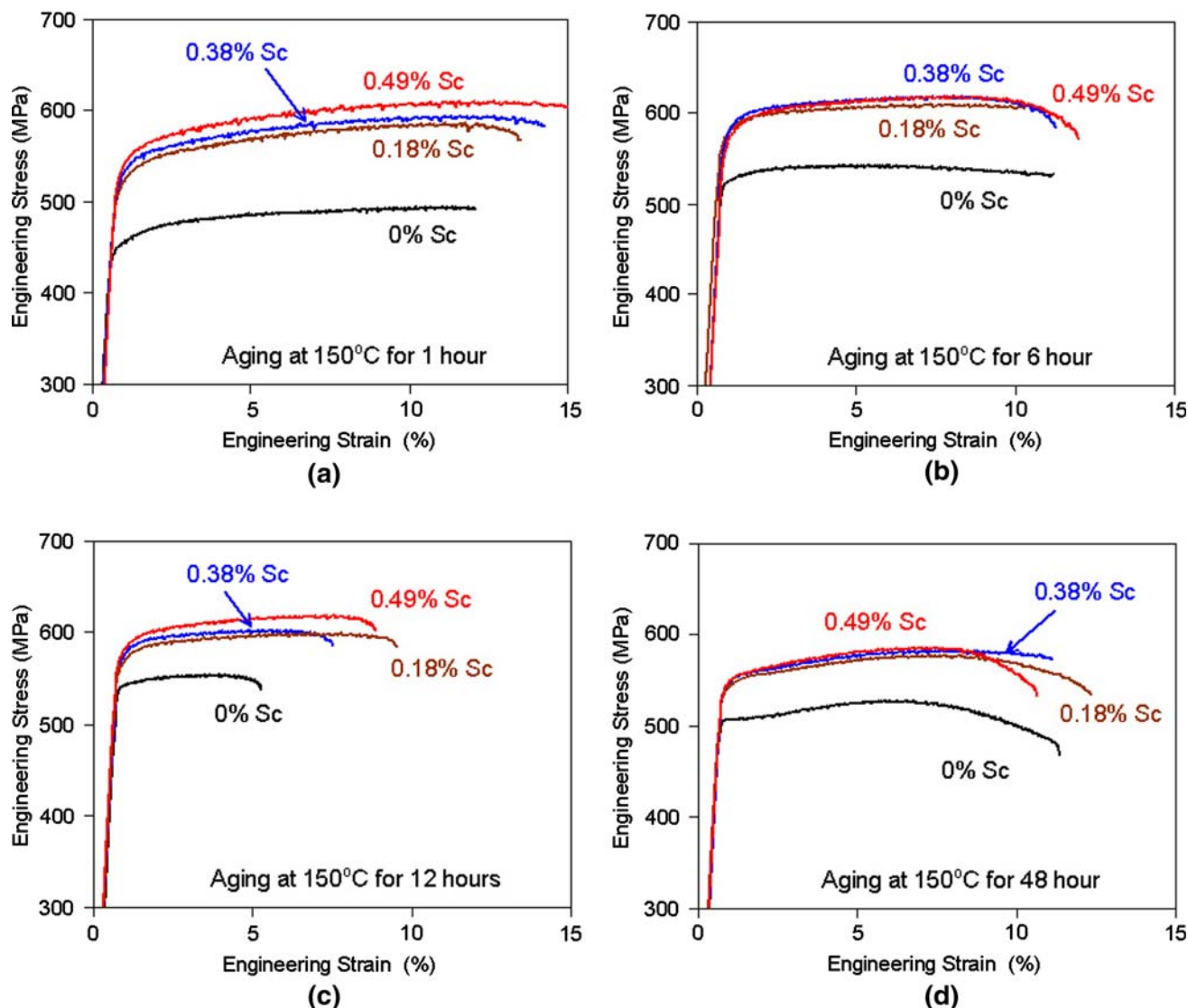


Fig. 18—RT stress-strain curves of DC-cast alloys SSA000, SSA018, SSA038, and SSA048 after solution treatment and artificial aging at 150 °C for (a) 1, (b) 6, (c) 12, and (d) 48 h.

**Table IV. RT Tensile Properties of the DC-Cast SSA Alloys after Solution Treatment and Natural Aging for 0.2 and 192 Hours**

Aging Time (h)	Alloy	YS (MPa)	UTS (MPa)	El (Pct)
0.2	SSA000	155	305	26
	SSA018	191	372	26
	SSA038	219	407	24
	SSA048	224	410	24
192	SSA000	285	421	25
	SSA018	362	534	25
	SSA038	371	546	20
	SSA048	374	559	21

lose their coherency at a smaller particle size than do the  $\text{Al}_3(\text{Sc,Zr})$  particles.<sup>[40,41]</sup> Additional study involving HRTEM is required to identify the coherency level of the matrix/particle interfaces. After solution treatment

and water quenching to RT, and during the following aging, no further evolution of both  $\text{Al}_3(\text{Sc,Zr})$  and  $\text{Al}_3\text{Zr}$  particles occurs. Thus, the fine coherent  $\text{Al}_3(\text{Sc,Zr})$  particles precipitated during solution treatment are evidently responsible for the higher strength of the Sc-containing alloys relative to the strength of the Sc-free alloy.

Very small amounts of Zr (about 0.037 wt pct or 0.011 at. pct<sup>[42]</sup>) and Sc (about 0.038 wt. pct or 0.022 at. pct<sup>[43]</sup>) are still present in the equilibrium solid solution during solution treatment at  $T = 460^\circ\text{C}$ ; these amounts of Zr and Sc are retained in the supersaturated solution after water quenching and may affect the kinetics of precipitation of GP zones and  $\eta'$  particles during aging. For example, the addition of Zr as a grain-refining element to Al-Zn-Mg alloys has been reported in earlier work<sup>[16,17]</sup> to retard and suppress the formation of GP zones at RT and, subsequently, to reduce the nucleation of  $\eta'$  during artificial aging at 135 °C.



**Table V. RT Tensile Properties of DC-Cast SSA Alloys after Solution Treatment and Artificial Aging at 120 °C for Different Time Periods**

Aging Time (h)	Alloy	YS (MPa)	UTS (MPa)	El (Pct)
8	SSA000	457	525	12
	SSA018	513	577	11
	SSA038	522	599	9
	SSA048	525	616	9
24	SSA000	487	547	11
	SSA018	543	620	10
	SSA038	551	625	9
	SSA048	550	635	9
162	SSA000	517	544	7
	SSA018	567	614	10
	SSA038	580	622	9
	SSA048	583	634	9
720	SSA000	522	540	8
	SSA018	545	589	10
	SSA038	559	601	10
	SSA048	562	609	9

**Table VI. RT Tensile Properties of DC-Cast SSA Alloys after Solution Treatment and Artificial Aging at 150 °C for Different Time Periods**

Aging Time (h)	Alloy	YS (MPa)	UTS (MPa)	El (Pct)
1	SSA000	440	495	13
	SSA018	506	587	12
	SSA038	519	597	14
	SSA048	526	610	14
6	SSA000	512	543	12
	SSA018	557	614	12
	SSA038	560	614	10
	SSA048	557	617	15
12	SSA000	537	553	6.5
	SSA018	554	601	9.5
	SSA038	558	602	8.0
	SSA048	560	605	9.5
48	SSA000	504	534	16
	SSA018	525	577	10
	SSA038	533	580	11
	SSA048	535	587	12

These negative effects of the Zr additions have been attributed to an increase in the number of vacancy sinks (due to the Zr-induced refined microstructure and the presence of semicoherent or incoherent  $\text{Al}_3\text{Zr}$ /matrix interfaces) and vacancy traps by Zr solute atoms (due to the high Zr-vacancy-binding energy in aluminum).<sup>[16,17]</sup> However, a recent study<sup>[15]</sup> has reported that the added Zr does not have any effect on the kinetics of the GP I zone formation at RT and at 100 °C, that it slows formation of the GP II zones at RT during the first 168 hours after quenching, that it accelerates precipitation of GP II at longer aging times at RT and during artificial aging at 100 °C, and that it slows the formation and growth of the  $\eta'$  phase within the first 20 hours of aging at 100 °C. These Zr effects on the precipitation kinetics in an Al-Zn-Mg alloy, which were reported in Reference 15, look similar to the Sc effects observed in

the present work. However, the effects of Sc on the precipitation processes in the Al-Zn-Mg-Cu-Zr alloy are quite different from the precipitation behavior in a Cu- and Sc-free, low-Mg alloy Al-Zn-Mg-Zr reported in the earlier work.<sup>[16,17]</sup>

To understand the discrepancy, we have conducted a critical analysis of the DSC thermograms of the naturally aged Al-Zn-Mg and Al-Zn-Mg-Zr alloys presented in the earlier work.<sup>[16,17]</sup> It was noticed that the intensities of the endothermic peaks related to the dissolution of GP zones formed during the 100-hour natural aging are slightly higher in the Zr-containing alloys than in Zr-free alloys (Figure 1(b) in Reference 16 and compare Figures 1(b) and 6(b) in Reference 17). Because the higher peak intensities are directly related to the higher volume fractions of the GP zones, this observation indicates that Zr did not really suppress the formation of GP zones at RT, as was claimed in References 16 and 17, but it slightly accelerated this process, probably due to the accelerating formation of GP II, which is now in line with the recent work.<sup>[15]</sup> The different precipitation behavior of the Zr-containing alloys during artificial aging reported in References 15 and 17 can be due to different aging temperatures (100 °C and 135 °C, respectively), different numbers of vacancy sinks (with respect to the subgrain structure), and different Mg contents. Different fractions of the coherent and noncoherent matrix/ $\text{Al}_3\text{Zr}$  interfaces formed after different hot-working processes may also result in the different behavior, because larger fractions of the noncoherent interfaces accelerate the annihilation rate of the excess vacancies. The Zr-induced (and Sc-induced) accelerated precipitation of the GP II zones observed in the Al-Zn-Mg alloys does not, however, support the point of view<sup>[16,17]</sup> that the traces of Zr (and, therefore, Sc or any other element with high solute-vacancy-binding energy) trap vacancies in the solid solution of these alloys and thus reduce the mobility of the vacancies, which are necessary for the diffusion of solute atoms to the GP zones. If this, indeed, happened, the formation of the GP II zones should slow down but not accelerate with the Zr and Sc additions in these alloys. Using a simple model for the solute-vacancy interactions, we will show that the traces of Zr and Sc do not decrease, but actually increase, the concentration of the quenched-in excess vacancies; they may also increase the number density of VRCs, in the Al-Zn-Mg based alloys.

It is well known<sup>[44]</sup> that the equilibrium concentration of vacancies in solid solution,  $C_V$ , is higher than in pure metal,  $C_V^p$ .<sup>†</sup> This is because the concentration of

<sup>†</sup>Here and thereafter, the vacancy concentration is identified as the fraction of the empty atom sites in the unit volume of the crystal matrix.

vacancies near a solute atom is increased by a factor of  $\exp(E_{S-V}/kT)$  over their concentration in the pure metal. Here,  $E_{S-V}$  is the solute-vacancy-binding energy and  $k$  is the Boltzmann constant. The  $C_V$  can, therefore, be defined as the sum of the concentrations of unbound (free) vacancies,  $C_{UV}$ , and solute-bound vacancies,  $C_{BV}$ .

The fraction of the bound vacancies increases with an increase in the concentration of the solute elements. Quenching from a high temperature provides a very high concentration of excess vacancies (both free and bound) that are believed to play an important part in the formation of GP clusters, due to the accelerating diffusion of the precipitate-forming elements aiming to replace the excess vacancies. Therefore, it is worthwhile to estimate how solute elements, including Zr and Sc, would affect the formation of the excess vacancies in the studied Al-Zn-Mg-Cu alloys.

The equilibrium concentration of vacancies in the studied alloys at a solution-treatment temperature (~460 °C) and at RT (25 °C) can be very approximately estimated by using the following formula:<sup>[44,45]</sup>

$$C_V = C_V^p \left\{ 1 - 12 \left( \sum_1^n C_i \right) + 12 \left[ \sum_1^n C_i \exp(E_{S_i-V}/kT) \right] \right\} \quad [2]$$

where  $C_V^p = 11.5 \exp(-E_V^{\text{Al}}/kT)$  is the equilibrium concentration of vacancies in pure Al at a temperature  $T$ ;  $E_V^{\text{Al}} = 0.76$  eV is the energy of the vacancy formation in pure Al;<sup>[46]</sup> and  $C_i$  is the atomic fraction of the  $i$ th alloying element. At 460 °C and at 25 °C,  $C_V^p$  is expected to be  $6.78 \times 10^{-5}$  and  $1.58 \times 10^{-12}$ , respectively.<sup>[46]</sup> The equilibrium concentration of vacancies trapped by an alloying element  $i$  is estimated as

$$C_{BV}^i = 12C_VC_i \exp(E_{S_i-V}/kT) \quad [3]$$

It is necessary to point out that Eqs. [2] and [3] have been derived under several assumptions (for details, see References 44 and 45) and, therefore, the values obtained using these equations must be considered only as very approximate qualitative estimations. The values of the solute-vacancy-binding energies for Zn, Mg, Cu, and Zr in the aluminum matrix have been reported to be 0.1, 0.19, 0.05, and 0.30 eV (Table III in Reference 45). The vacancy-binding energy for Sc has recently been determined to be  $E_{\text{Sc}-V} = 0.35$  eV.<sup>[47]</sup> However, this value is slightly overestimated because  $E_V^{\text{Al}} = 0.79$  eV was used in Reference 47, while in the calculations of the solute-vacancy-binding energies for all other elements,  $E_V^{\text{Al}} = 0.76$  eV was used. At this latter value of  $E_V^{\text{Al}}$ , the Sc-vacancy-binding energy is estimated to be 0.33 eV. Using this corrected value for Sc, as well as the reported solute-vacancy-binding energies for Zn, Mg, Cu, and Zr, the equilibrium concentrations of vacancies in the SSA000 (0 pct Sc) and SSA038 (0.38 pct Sc) alloys at the solution-treatment temperature (460 °C) and at RT (25 °C) were estimated and the values are given in Table VII. The concentrations of Zr and Sc in the Al solid solution at 460 °C were taken to be 0.012 and 0.020 at. pct, respectively. It was also assumed that, immediately after water quenching, these elements, as well as Zn, Mg, and Cu, were retained in the supersaturated solid solution. To estimate the effect of Zr on the vacancy concentrations, an alloy SSA000m, which has the same composition as alloy SSA000 but without the Zr, is also shown in Table VII.

**Table VII. Atomic fractions of Alloying Elements in FCC-Al Phase at 460 °C and Calculated Concentrations of Equilibrium Vacancies at 460 °C and 25 °C;  $C_V$ ,  $C_{BV}$ , and  $C_{UV}$  Are the Concentrations of Total, Total Bound, and Total Unbound Vacancies, Respectively, and  $C_{BV}^{M_i}$  Is the Concentration of the Bound Vacancies Associated with an Element  $M_i$ , where  $M_i$  is Zn, Mg, Cu, Zr, or Sc**

	SSA000m	SSA000	SSA038
Atomic fractions of alloying elements			
Zn	$3.10 \times 10^{-2}$	$3.10 \times 10^{-2}$	$3.10 \times 10^{-2}$
Mg	$2.69 \times 10^{-2}$	$2.69 \times 10^{-2}$	$2.69 \times 10^{-2}$
Cu	$7.21 \times 10^{-3}$	$7.21 \times 10^{-3}$	$7.21 \times 10^{-3}$
Zr	0	$1.10 \times 10^{-4}$	$1.10 \times 10^{-4}$
Sc	0	0	$2.20 \times 10^{-4}$
Calculated equilibrium vacancy concentrations at $T = 460$ °C			
$C_V$	$5.95 \times 10^{-4}$	$6.05 \times 10^{-4}$	$6.39 \times 10^{-4}$
$C_{BV}$	$5.80 \times 10^{-4}$	$5.91 \times 10^{-4}$	$6.24 \times 10^{-4}$
$C_{UV}$	$1.48 \times 10^{-5}$	$1.47 \times 10^{-5}$	$1.46 \times 10^{-5}$
$C_{BV}^{\text{Zn}}$	$1.23 \times 10^{-4}$	$1.23 \times 10^{-4}$	$1.23 \times 10^{-4}$
$C_{BV}^{\text{Mg}}$	$4.44 \times 10^{-4}$	$4.44 \times 10^{-4}$	$4.44 \times 10^{-4}$
$C_{BV}^{\text{Cu}}$	$1.30 \times 10^{-5}$	$1.30 \times 10^{-5}$	$1.30 \times 10^{-5}$
$C_{BV}^{\text{Zr}}$	0	$1.04 \times 10^{-5}$	$1.04 \times 10^{-5}$
$C_{BV}^{\text{Sc}}$	0	0	$3.34 \times 10^{-5}$
Calculated equilibrium vacancy concentrations at $T = 25$ °C			
$C_V$	$8.67 \times 10^{-10}$	$1.12 \times 10^{-9}$	$2.72 \times 10^{-9}$
$C_{BV}$	$8.67 \times 10^{-10}$	$1.12 \times 10^{-9}$	$2.72 \times 10^{-9}$
$C_{UV}$	$3.45 \times 10^{-13}$	$3.43 \times 10^{-13}$	$3.39 \times 10^{-13}$
$C_{BV}^{\text{Zn}}$	$2.44 \times 10^{-10}$	$2.44 \times 10^{-10}$	$2.44 \times 10^{-10}$
$C_{BV}^{\text{Mg}}$	$8.37 \times 10^{-10}$	$8.37 \times 10^{-10}$	$8.37 \times 10^{-10}$
$C_{BV}^{\text{Cu}}$	$9.58 \times 10^{-13}$	$9.58 \times 10^{-13}$	$9.58 \times 10^{-13}$
$C_{BV}^{\text{Zr}}$	0	$2.49 \times 10^{-10}$	$2.49 \times 10^{-10}$
$C_{BV}^{\text{Sc}}$	0	0	$1.60 \times 10^{-9}$

The results given in Table VII demonstrate that, at  $T = 460$  °C, about 98 pct of all equilibrium vacancies are solute-bound vacancies and only 2 pct are free vacancies. Small additions of Zr or Sc form additional solute-bound vacancies, and the total concentration of the bound vacancies increases (from  $5.95 \times 10^{-4}$  in the alloy without Zr and Sc to  $6.05 \times 10^{-4}$ , when Zr is added, and to  $6.39 \times 10^{-4}$ , when both Zr and Sc are added), while the concentration of the free vacancies slightly decreases (from  $1.48 \times 10^{-5}$  to  $1.47 \times 10^{-5}$  and to  $1.46 \times 10^{-5}$ , respectively). The concentrations of the vacancies attached to Mg, Zn, and Cu do not change with the Zr and Sc additions. The increase in the total vacancy concentration at 460 °C by the Zr and Sc additions is almost completely due to an increase in the concentration of the bound vacancies. The equilibrium concentration of vacancies at  $T = 25$  °C is about five orders of magnitude less than that at 460 °C, and almost all these vacancies are the solute-bound vacancies.

Because their concentration at 460 °C is much higher than at RT, almost all high-temperature free and bound vacancies become quenched-in excess vacancies after alloy quenching. These quenched-in vacancies can produce VRCs and can also accelerate the diffusion of

atoms toward the formerly vacancy-bound solutes. The quenched-in excess free vacancies, whose concentration is about four orders of magnitude higher than that of the equilibrium vacancy concentration at RT, will accelerate the cluster growth just after quenching; the rate of the release of the quenched-in excess bound vacancies, the concentration of which is about  $5 \times 10^5$  times higher than the equilibrium concentration at RT, will control the rate of the cluster growth during an extended period of time.

From this analysis, two main types of VRCs are expected: the Mg-bound excess vacancies produce Mg-rich GP I clusters and the Zn-bound excess vacancies produce Zn-rich GP II clusters. This agrees with a recent report<sup>[11]</sup> that the formation of both GP I and GP II clusters is assisted by quenched-in vacancies. Assuming that all quenched-in excess bound vacancies associated with Mg and Zn produce the GP clusters, the maximum number densities of the Mg-rich ( $N_{\text{VRC}}^{\text{Mg}}$ ) and Zn-rich ( $N_{\text{VRC}}^{\text{Zn}}$ ) clusters, which can be formed in the fcc Al matrix (the lattice parameter  $a \approx 0.403$  nm,  $\sim 6.1 \times 10^{22}$  atom sites per  $\text{cm}^3$ ) after quenching from 460 °C, are estimated to be  $N_{\text{VRC}}^{\text{Mg}} \approx 2.7 \times 10^{19} \text{ cm}^{-3}$  and  $N_{\text{VRC}}^{\text{Zn}} \approx 7.5 \times 10^{18} \text{ cm}^{-3}$ . These estimated numbers agree very well with the recently reported, experimentally determined total number density of  $\sim 6 \times 10^{19} - 9 \times 10^{19} \text{ cm}^{-3}$  of the GP clusters formed after quenching,<sup>[11]</sup> thereby validating our simple model.

If Zr or Sc are present in the alloy, the quenched-in excess solute-bound vacancies associated with these atoms will also form VRCs after quenching and will enhance the atom flux to these clusters. The number densities of these clusters are estimated to be  $N_{\text{VRC}}^{\text{Zr}} \approx 6.3 \times 10^{17} \text{ cm}^{-3}$  and  $N_{\text{VRC}}^{\text{Sc}} \approx 2.0 \times 10^{18} \text{ cm}^{-3}$ . We are suggesting that these Zr- and Sc-rich clusters are responsible for the accelerated formation and growth of GP II and  $\eta'$  during artificial aging. This suggestion is based on the fact that both Zr and Sc can form a number of Zn-rich intermetallic phases (*i.e.*,  $\text{Zn}_{14}\text{Zr}$ ,  $\text{Zn}_{22}\text{Zr}$ ,  $\text{Zn}_{12}\text{Sc}$ , and  $\text{Zn}_4\text{Sc}$ ).<sup>[48]</sup> Formation of these phases during aging is unlikely, because of the extremely low diffusivity of Sc and Zr; however, the VRCs containing the Zr and Sc atoms will attract faster-diffusing Zn atoms and, eventually, will transform to the Zn-rich VRCs. Using the values given in Table VII, it is estimated that the Zr addition can provide up to an 8.4 pct increase in the number density of the Zn-rich VRCs and an approximately 1.7 pct increase in the number of the quenched-in excess vacancies, to transform these VRCs into GP II zones or  $\eta'$  particles during aging. The further Sc addition can give an additional 26 pct increase in the number density of the Zn-rich VRCs and an approximately 5.2 pct increase in the number of the quenched-in excess vacancies.

The proposed model of the Sc (and Zr) effects on the concentration of the quenched-in excess vacancies and on the formation of the Mg-rich and Zn-rich clusters effectively explains the aging behavior of the Sc-containing Al-Zn-Mg-Cu alloys reported in the present work and of the Zr-containing Al-Zn-Mg alloys reported in References 15, 16, and 17. Indeed, during the natural aging of the Al-Zn-Mg-Cu SSA series alloys,

only GP I zones are developed from Mg-rich clusters. With respect to our model, the number density of these clusters and the concentration of the quenched-in Mg-bound excess vacancies are the same in the Sc-free and Sc-containing alloys. A decrease in the concentration of the quenched-in free excess vacancies (from  $1.47 \times 10^{-5}$  to  $1.46 \times 10^{-5}$ ) due to the Sc in solid solution is very small, as well (Table VII). Because of the spherical nature of the GP I zones and their full coherency with the matrix, they should mainly produce hydrostatic strains. Therefore, only a very weak, if any, interaction of these spherical zones with the fine coherent spherical  $\text{Al}_3(\text{Sc,Zr})$  particles can be expected.<sup>[49]</sup> This explains why the presence of the Sc in the form of a supersaturated solid solution and coherent  $\text{Al}_3(\text{Sc,Zr})$  particles does not have any effect on the kinetics of natural aging in these alloys.

The main difference in the artificial aging at 120 °C and 150 °C, as compared to the natural aging, is that GP II zones and  $\eta'$  particles become major precipitates; peak aging is also reached, followed by overaging, when  $\eta$  particles form and grow. Although GP I zones are still present at the early stages of aging at 120 °C in both the Sc-free and Sc-containing alloys, these zones dissolve completely (or partially transform to  $\eta'$ , in accordance with Reference 10) after a 24-hour aging at 120 °C, and they are not detected at all after aging at 150 °C. The GP II zones are known to nucleate on the Zn-rich VRCs, which are resistant to growing at temperatures below 70 °C.<sup>[6-8,11]</sup> The concentration of Zn rapidly decreases with an increase in the GP II zone size, due to the addition of Mg and Al,<sup>[11]</sup> and, at the Zn:Mg ratio close to 1.0 to 1.2, GP II seems to transform to coherent  $\eta'$  particles of similar composition.<sup>[8,11,50]</sup> The  $\eta'$  particles may also nucleate directly from the Zn-rich VRCs.<sup>[12,14]</sup> Because the formation of both the GP II and the  $\eta'$  is directly related to the Zn-rich vacancy clusters, a higher number density of these clusters in the Sc-containing alloys, as predicted by our model, can be one of the reasons for the accelerated aging of the Sc-containing alloys during early stages at 120 °C and 150 °C (Figure 15 and Tables V and VI).

A slightly different aging behavior at 120 °C and 150 °C can be explained by different sequences in the precipitation and growth of GP II zones and  $\eta'$  particles. Aging at 120 °C starts with the formation of the GP II zones. In accordance with our model, the number density of these zones is higher and these zones should grow faster, due to the higher concentration of the quenched-in solute-bound excess vacancies in the Sc-containing alloys. This causes a more rapid increase in the microhardness in the Sc-containing alloys, at the early stages of artificial aging at 120 °C. However, because of the faster growth of the GP II zones, these zones start to transform to the  $\eta'/\eta$  particles after shorter aging times in the Sc-containing alloys, which leads to a slowing of the aging process in the Sc-containing alloys above 8 hours; in the Sc-free alloy, the aging process continues at an almost constant rate. It is also possible that internal stresses from  $\text{Al}_3(\text{Sc,Zr})$  particles stabilize the GP II zones, so that they grow to a larger size before they start to transform to the  $\eta'$  particles. This would



lead to larger  $\eta'$  particles and an earlier transformation to  $\eta$  particles in the Sc-containing alloys. Both the slowing of the rate of the particle growth with an increase in the particle size and the earlier formation of the  $\eta$  particles can be reasons for the slowing of the aging process in the Sc-containing alloys at the aging times above 8 hours, while the peak-aging condition is achieved after approximately the same aging time, at ~160 hours, independent of the Sc content. The presence of Sc probably does not affect the kinetics of the growth of the  $\eta$  particles, because the difference in the microhardness of the Sc-free and Sc-containing alloys barely changes with an increase in the overaging time.

Aging at 150 °C starts from the formation of the  $\eta'$  particles, and the presence of Sc results in a slightly accelerated formation and growth of these particles. Such behavior can also be explained by the higher number density of the VRCs in the Sc-containing alloys; this is similar to the situation that occurs during aging at 120 °C. Since the  $\eta'$  particles are found to be the main precipitates at early stages (within ~0.5 to 6 hours) of aging at 150 °C, the microhardness and strength increase faster in Sc-containing alloys than in the Sc-free alloy. At longer aging times (6 to 12 hours), the aging response of the Sc-containing alloys slows, due to the faster coarsening of the  $\eta'$  particles and their transformation into the equilibrium  $\eta$  particles. An increase in the volume fraction of the  $\eta$  phase and the coarsening of the  $\eta'$ - and  $\eta$ -phase particles seem to be responsible for a decrease in the microhardness and strength in the overaged condition, unaided by the presence of Sc.

While effectively explaining the effects of Sc on the aging of the Al-Zn-Mg-Cu alloys, the proposed model also highlights the importance of the solution-treatment temperature. In particular, the model predicts that a higher concentration of quenched-in vacancies, a higher number density of GP clusters, and different fractions of the GP I and GP II clusters can be produced using a higher solution-treatment temperature (*e.g.*, the fraction of GP II clusters should increase with an increase in the solution-treatment temperature).

## V. CONCLUSIONS

The following conclusions can be drawn from our study.

1. The effect of small additions of Sc and Zr on the microstructure and properties of a DC-cast Al-Zn-Mg-Cu alloy after solution treatment and aging was studied. After DC casting, no primary  $\text{Al}_3\text{Zr}$  or  $\text{Al}_3(\text{Sc},\text{Zr})$  particles were observed in alloys SSA000 (0.17 pct Zr, 0 pct Sc) and SSA018 (0.18 pct Zr, 0.18 pct Sc), while these particles were detected in alloys SSA038 (0.17 pct Zr, 0.38 pct Sc) and SSA048 (0.14 pct Zr, 0.49 pct Sc). No secondary  $\text{Al}_3\text{Zr}$  and  $\text{Al}_3(\text{Sc},\text{Zr})$  precipitates were found in any of the four alloys after the casting and before the heat treatment. These results indicate that at least 0.18 pct Sc and 0.17 pct Zr were in a supersaturated solid solution in these alloys after the casting.

Solution treatment led to the precipitation of fine  $\text{Al}_3\text{Zr}$  and  $\text{Al}_3(\text{Sc},\text{Zr})$  dispersoids from the supersaturated solid solution. The presence of these dispersoids provided an increase in the YS from 155 to 224 MPa, in the UTS from 305 to 410 MPa, and in the microhardness from  $H_v = 0.85$  to 0.98 GPa in the freshly solution-heat-treated condition. The strength and hardness values increased further after the precipitation of metastable Zn and Mg containing precipitates during natural or artificial aging.

2. Scandium had no effect on natural aging. In both Sc-free and Sc-containing alloys, the natural aging was controlled by the formation and growth of GP I zones, and the alloys showed similar precipitation kinetics. This led to the same increase in hardness and tensile strength in the Sc-free and Sc-containing alloys after being held at RT for the same period of time. After holding at RT for 192 hours, the alloy without Sc had YS = 285 MPa, UTS = 421 MPa, and  $H_v = 1.44$  GPa, while the alloy with 0.38 pct Sc had YS = 371 MPa, UTS = 546 MPa, and  $H_v = 1.57$  GPa.
3. Scandium accelerated the aging process within the first 8 hours at 120 °C, due to the more rapid formation and growth of the GP II zones. However, at longer aging times, when the GP II zones transformed to  $\eta'$  and  $\eta$  particles, the aging response of the Sc-containing alloys slowed down. After a ~162-hour aging (*i.e.*, in the peak-aged condition), the difference in the hardness of the alloys with and without Sc were minimal. On the other hand, the difference in the YS and UTS of these alloys remained almost unchanging. In the peak-aged condition, the alloy without Sc had  $H_v = 2.07$  GPa, YS = 517 MPa, and UTS = 544 MPa, while the alloy with 0.38 pct Sc had  $H_v = 2.05$  GPa, YS = 580 MPa, and UTS = 622 MPa. During overaging, which was controlled by the formation and growth of  $\eta$  particles, the Sc-free and Sc-containing alloys had almost the same microhardness but different tensile strength values. The difference in the tensile strengths decreased with an increase in the overaging time.
4. Aging at 150 °C was controlled by the formation and growth of the  $\eta'$  particles within the first 0.5 to 6 hours and by the formation and growth of  $\eta$  particles at longer times. The presence of Sc resulted in an accelerated formation and growth of  $\eta'$  particles, which led to a more rapid increase in the hardness and strength in the Sc-containing alloys during the early stage of aging at 150 °C. However, the aging response of the Sc-containing alloys slowed down at longer aging times (6 to 12 hours), due to the faster coarsening of the  $\eta'$  particles and their transformation to  $\eta$  particles. In the peak-aging condition, the difference in the hardness and strength of the alloys with and without Sc was minimal. For example, after aging at 150 °C for 12 hours, the alloy without Sc had  $H_v = 2.04$  GPa, YS = 537 MPa, and UTS = 553 MPa; the alloy with 0.38 pct Sc had  $H_v = 2.08$  GPa, YS = 558 MPa, and UTS = 602 MPa. During overaging, both the microhardness



and the strength of the alloys decreased, due to the coarsening of the  $\eta'/\eta$ -phase particles and the increasing volume fraction of the  $\eta$  particles.

## ACKNOWLEDGMENTS

The authors thank Drs. D.B. Miracle and C.F. Woodward, United States Air Force Research Laboratory (Wright-Patterson Air Force Base, OH), Dr. R. Wheeler, UES, Inc. (Dayton, OH), and Prof. M. Mills, Ohio State University (Columbus, OH), for useful technical help and discussions. This work was financially supported through the United States Air Force Contracts Nos. F04611-02-C-0014 (Capt. William Allen, Program Manager) and FA8650-04-D-5233 (Dr. Joan Fuller, Program Manager).

## REFERENCES

1. *Properties of Aluminum Alloys: Tensile, Creep, and Fatigue Data at High and Low Temperatures*, J.G. Kaufman, ed., ASM INTERNATIONAL, Materials Park, OH, 1999.
2. *Aluminum and Aluminum Alloys*, J.R. Davis, ed., ASM INTERNATIONAL, Materials Park, OH, 1993.
3. J.H. Auld and S.McK. Cousland: *J. Austr. Inst. Met.*, 1974, vol. 19, pp. 194–99.
4. F.A. Costello, J.D. Robson, and P.B. Pragnell: *Mater. Sci. Forum*, 2002, vols. 396–402, pp. 757–62.
5. P. Villars and L.D. Calvert: *Pearson's Handbook of Crystallographic Data for Intermetallic Phases*, ASM INTERNATIONAL, Materials Park, OH, 1991, vols. 1–4.
6. K. Stiller, P.J. Warren, V. Hansen, J. Angenete, and J. Gjønnes: *Mater. Sci. Eng., A*, 1999, vol. A270, pp. 55–63.
7. L.K. Berg, J. Gjønnes, V. Hansen, X.Z. Li, M. Knutson-Wedel, G. Waterloo, D. Schryvers, and L.R. Wallenberg: *Acta Mater.*, 2001, vol. 49, pp. 3443–51.
8. T. Engdahl, V. Hansen, P.J. Warren, and K. Stiller: *Mater. Sci. Eng., A*, 2002, vol. A327, pp. 59–64.
9. V. Hansen, O.B. Karlsen, Y. Langsrud, and J. Gjønnes: *Mater. Sci. Technol.*, 2004, vol. 20, pp. 185–93.
10. G. Sha and A. Cerezo: *Acta Mater.*, 2004, vol. 52, pp. 4503–16.
11. A. Dupasquier, R. Ferragut, M.M. Iglesias, M. Massazza, R. Riontino, P. Mengucci, G. Barucca, C.E. Macchi, and A. Somoza: *Philos. Mag.*, 2007, vol. 87, pp. 3297–3323.
12. H. Löffler, I. Kovács, and J. Lendvai: *J. Mater. Sci.*, 1993, vol. 18, pp. 2215–40.
13. X.Z. Li, V. Hansen, J. Gjønnes, and R. Wallenberg: *Acta Mater.*, 1999, vol. 47, pp. 2651–59.
14. *Handbook of Aluminum*, G.E. Totten and D.S. MacKenzie, eds., Marcel Dekker, Inc., New York, NY, 2003, vol. 1, pp. 284–89 and 916–20.
15. X.J. Jiang, B. Noble, V. Hansen, and J. Taftø: *Metall. Mater. Trans. A*, 2001, vol. 32, pp. 1063–73.
16. A.K. Mukhopadhyay, G.J. Shiflet, and S.R. Starke: *Scripta Mater.*, 1990, vol. 24, pp. 307–12.
17. A.K. Mukhopadhyay, Q.B. Yang, and S.B. Singh: *Acta Metall. Mater.*, 1994, vol. 42, pp. 3083–91.
18. V.I. Elagin: *Technology of Light Alloys*, Tekhnologiya Legkikh Splavov, USSR, 1994, No. 9, pp. 5–14.
19. V.I. Elagin, V.V. Zakharova, and T.D. Rostova: *Met. Sci. Heat Treat.*, 1995, vol. 36 (7–8), pp. 375–80.
20. O.N. Senkov, R.B. Bhat, and S.V. Senkova: in *Metallic Materials with High Structural Efficiency*, O.N. Senkov, D.B. Miracle, and S.A. Firstov, eds., Kluwer Academic Publishers, Dordrecht, The Netherlands, 2004, pp. 151–62.
21. Y.V. Milman, A.I. Sirko, D.V. Lotsko, D.B. Miracle, and O.N. Senkov: *Mater. Sci. Forum*, 2002, vols. 396–402, pp. 1217–22.
22. A.F. Norman, K. Hyde, F. Costello, S. Thompson, S. Birley, and P.B. Pragnell: *Mater. Sci. Eng., A*, 2003, vol. 354, pp. 188–98.
23. O.N. Senkov, R.B. Bhat, S.V. Senkova, and J.D. Schloz: *Metall. Mater. Trans. A*, 2005, vol. 36A, pp. 2115–26.
24. J. Royset and N. Ryum: *Int. Mater. Rev.*, 2005, vol. 50, pp. 19–44.
25. O.N. Senkov: *Advanced Aluminum Materials for Rocket Turbopump Rotors*, SBIR Phase II Final Report, AFRL-PR-ED-TR-2006-0073, U.S. Air Force Research Laboratory, Edwards Air Force Base, CA, 2006, pp. 205–30.
26. O.N. Senkov, S.V. Senkova, M.G. Mendiratta, and D.B. Miracle: U.S. Patent 7,048,815, 2006.
27. O.N. Senkov, S.V. Senkova, M.G. Mendiratta, D.B. Miracle, Y.V. Milman, D.V. Lotsko, and A.I. Sirko: U.S. Patent 7,060,139, 2006.
28. L.I. Kaigorodova, E.I. Selnikhina, E.A. Tkachenko, and O.G. Senatorova: *Phys. Met. Metall.*, 1996, vol. 81, pp. 513–19.
29. Y.L. Wu, F.H. Froes, C. Li, and A. Alvarez: *Metall. Mater. Trans. A*, 1999, vol. 30A, pp. 1017–24.
30. D.B. Williams and C.B. Carter: *Transmission Electron Microscopy*, Plenum Press, New York, NY, 1996, pp. 629–30.
31. S. Iwamura and Y. Miura: *Acta Mater.*, 2004, vol. 52, pp. 591–600.
32. R. DeIasi and P.N. Adler: *Metall. Trans. A*, 1977, vol. 8A, pp. 1177–83.
33. P.H. Adler and R. DeIasi: *Metall. Trans. A*, 1977, vol. 8A, pp. 1185–90.
34. J.M. Papazian, R.J. DeIasi, and P.N. Adler: *Metall. Trans. A*, 1980, vol. 11A, pp. 135–40.
35. J.M. Papazian: *Metall. Trans. A*, 1982, vol. 13A, pp. 761–69.
36. A. Deschamps, F. Livet, and Y. Brechet: *Acta Mater.*, 1999, vol. 47, pp. 281–92.
37. Y.H. Zhao, X.Z. Liao, Z. Jin, R.Z. Valiev, and Y.T. Zhu: *Acta Mater.*, 2004, vol. 51, pp. 4589–99.
38. *PANDAT™, Version 5.0*, CompuTherm, LLC, Madison, WI.
39. O.N. Senkov and M.R. Shaghiev: UES, Inc., Dayton, Ohio, unpublished research, 2006.
40. B.L. Ou, J.G. Yang, and M.Y. Wei: *Metall. Mater. Trans. A*, 2007, vol. 38A, pp. 1760–73.
41. S. Iwamura and Y. Miura: *Acta Mater.*, 2004, vol. 52, pp. 591–600.
42. J. Murray, A. Peruzzi, and J.P. Abriata: *J. Phase Equilib.*, 1992, vol. 13, pp. 277–91.
43. H.H. Jo and S.I. Fujikawa: *Mater. Sci. Eng.*, 1993, vol. A171, pp. 151–61.
44. J. Burke: *J. Less Common Met.*, 1972, vol. 28, pp. 441–56.
45. S. Özbilen and H.M. Flower: *Acta Metall.*, 1989, vol. 37, pp. 2993–3000.
46. R.O. Simmons and R.W. Balluffi: *Phys. Rev.*, 1960, vol. 117, pp. 52–61.
47. Y. Miura, C. Joh, and T. Katsube: *Mater. Sci. Forum*, 2000, vols. 331–337, pp. 1031–36.
48. O. Kubaschewski, C.B. Alcock, and P.J. Spencer: *Materials Thermochemistry*, 6th ed., Pergamon Press, Oxford, United Kingdom, 1993.
49. J.D. Eshelby: in *Solid State Physics*, F. Seitz and D. Turnbull, eds., Academic Press, New York, NY, 1956, vol. 3, pp. 77–144.
50. S.K. Maloney, K. Hono, I.J. Polmear, and S.P. Ringer: *Scripta Mater.*, 1999, vol. 41, pp. 1031–38.